

# Contents

<b>Introduction</b>	<b>iii</b>
<b>1 Neutrino physics overview</b>	<b>1</b>
1.1 Brief history of neutrinos . . . . .	1
1.2 Neutrinos in the Standard Model and neutrino masses . . . . .	2
1.2.1 Limits on neutrino masses . . . . .	4
1.3 Theory of neutrino oscillations . . . . .	5
1.3.1 Three flavours oscillations in vacuum . . . . .	6
1.3.2 Charge-parity symmetry violation . . . . .	7
1.3.3 Two flavor scenario . . . . .	9
1.3.4 MSW matter effects . . . . .	9
1.4 Neutrino oscillation experiments . . . . .	12
1.4.1 Solar experiments: $\theta_{12}$ and $\Delta m_{12}^2$ . . . . .	13
1.4.2 Reactor experiments . . . . .	16
1.4.3 Atmospheric experiments: $\Delta m_{31}^2$ and $\theta_{23}$ . . . . .	18
1.4.4 Accelerator experiments . . . . .	20
1.4.5 $\delta_{CP}$ experimental results . . . . .	21
1.4.6 Mass hierarchy experimental results . . . . .	22
1.5 State of the art and future prospects . . . . .	22
<b>2 DUNE</b>	<b>25</b>
2.1 DUNE's scientific program . . . . .	25
2.1.1 Sensitivities and systematics . . . . .	27
2.1.2 Mass ordering and $\delta_{CP}$ . . . . .	29
2.1.3 Precision measurements . . . . .	35
2.1.4 Proton decay measurements . . . . .	36
2.1.5 Supernova neutrino measurements . . . . .	38
2.1.6 Oscillation physics with atmospheric neutrinos . . . . .	39
2.1.7 Near detector physics . . . . .	40
2.2 LBNF/DUNE's facilities and design . . . . .	40
2.2.1 FD reference design: single phase LArTPC . . . . .	40

2.2.2	FD alternative design: double phase LArTPC . . . . .	45
2.2.3	LBNF beamline . . . . .	46
2.2.4	The near detector . . . . .	48
<b>3</b>	<b>SAND</b>	<b>51</b>
3.1	Requirements . . . . .	51
3.2	Detector components . . . . .	52
3.2.1	KLOE’s magnet . . . . .	52
3.2.2	KLOE’s electro-magnetic calorimeter . . . . .	53
3.2.3	The inner tracker . . . . .	55
3.3	Physics Program . . . . .	58
3.3.1	Reducing the systematics . . . . .	58
3.3.2	Precision measurements and new physics . . . . .	59
<b>4</b>	<b>The simulation</b>	<b>63</b>
4.1	GENIE: MC neutrino generator . . . . .	63
4.1.1	GENIE usage for the ND collaboration . . . . .	64
4.2	GGD: geometry generation tool . . . . .	67
4.2.1	SAND’s geometry and the ECAL . . . . .	67
4.3	Edep-sim: charged particle propagation . . . . .	71
4.4	Signal digitization . . . . .	72
4.4.1	The ECAL . . . . .	72
4.4.2	The STT . . . . .	75
4.5	Reconstruction . . . . .	76
4.5.1	Track reconstruction in the STT . . . . .	76
<b>5</b>	<b>Analysis and results</b>	<b>77</b>
	<b>Bibliografia</b>	<b>79</b>

# **Introduction**

Questa è l'introduzione.



# Chapter 1

## Neutrino physics overview

### 1.1 Brief history of neutrinos

Neutrinos made their first appearance in modern physics as an hypothetical particle proposed by W. Pauli in order to solve the problem related to the continuous energy spectrum measured for  $\beta$ -decay electrons [1]. It was given its name by Enrico Fermi, the first scientist to take in serious consideration Pauli's hypothesis and develop a theory of beta decay that included the new particle as one of the four fermions involved in the correspondent interaction [2]. Fermi's theory led Bethe and Peierls to the first estimation of the inverse interaction's cross section [3]:

$$\sigma(\bar{\nu}p \rightarrow ne^+) \leq 10^{-44} \text{ cm}^2, \quad E_{\bar{\nu}} \simeq 2 \text{ MeV} \quad (1.1)$$

The smallness of the cross section led the two scientists to conclude that it would be almost impossible to detect such an interaction.

B. Pontecorvo was the first to realize that with a neutrino flux of about  $10^{11} \nu/\text{cm}^2/\text{s}$ , of the order of the one produced by an average nuclear reactor, and pointing it towards a ton mass scale detector one could obtain a rate of a few events per day [4]. This idea was put into practice by Reines and Cowan, whose experiment led to the discovery of the anti-neutrino in 1956 [5]. Their technique for the identification of the  $\bar{\nu}$  relied on the detection of the light produced by the neutron capture, in delay with respect to the annihilation of the positron, a template still in use today.

In 1962 Lederman, Schwartz and Steinberger showed the existence of a second type of neutrino, associated with the muon in the main decay mode of the pion:  $\pi^- \rightarrow \mu^- \bar{\nu}_\mu$  [6]. This was also the first case in which an accelerator neutrino beam was used in any experiment. Such beam was generated by the decay of pions and other hadrons produced in the collision of accelerated

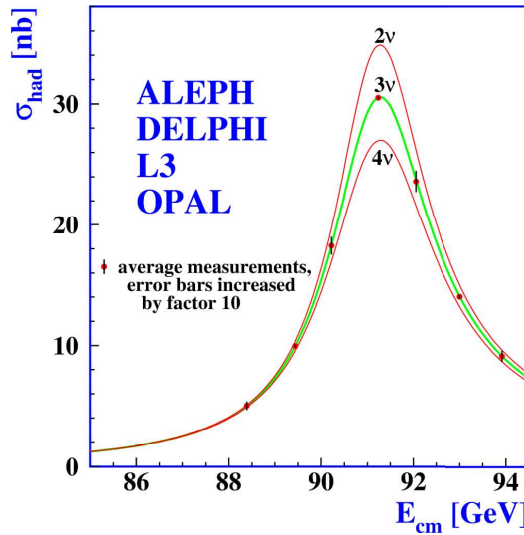


Figure 1.1: Theoretical predictions of the total cross-section for the production of hadrons as a function of the center of mass energy for 2, 3 and 4 neutrino families. Experimental data from LEP drawn as dots [7]

protons on a target. A neutrino detector revealed the leptons produced in the charged current (CC) interactions.

The  $\tau$  lepton was discovered at the SLAC accelerator in the seventies, and it would soon be argued that a third neutrino might be associated to it as for the lighter leptons. The study of the decay width of the  $Z_0$  produced at LEP in  $e^+e^-$  collisions showed that the number of light neutrinos coupled to the neutral weak boson was three (Fig. 1.1 ) [7]:

$$N_\nu = \frac{\Gamma_{inv}}{\Gamma_{\bar{\nu}\nu}} = 2.984 \pm 0.008 \quad (1.2)$$

The tau neutrino was finally discovered at Fermilab in 2001 at the DONUT experiment [8] by revealing the taus produced in CC interactions in iron.

## 1.2 Neutrinos in the Standard Model and neutrino masses

The Standard Model (SM) of particle physics is a gauge theory defined by the symmetry  $SU(3) \times SU(2)_L \times U(1)_Y$  with the subscripts L and Y indicating the left chirality of the particles and their hypercharge respectively. The  $SU(3)$  describes the quark interaction in the quark sector while  $SU(2)_L \times U(1)_Y$  is related to the electroweak sector.

$\begin{pmatrix} \nu_e \\ e \end{pmatrix}_L$	$\begin{pmatrix} u \\ d \end{pmatrix}_L$	$e_R \quad u_R \quad d_R$
$\begin{pmatrix} \nu_\mu \\ \mu \end{pmatrix}_L$	$\begin{pmatrix} c \\ s \end{pmatrix}_L$	$\mu_R \quad c_R \quad s_R$
$\begin{pmatrix} \nu_\tau \\ \tau \end{pmatrix}_L$	$\begin{pmatrix} t \\ b \end{pmatrix}_L$	$\tau_R \quad t_R \quad b_R$

Table 1.1: All irreducible fermion representations in the the SM.

The particles in the SM are divided into bosons of spin 1 that mediate the fundamental interactions (photons for the electromagnetic interactions,  $W^\pm$  and  $Z^0$  for the weak sector and 8 gluons for the strong sector), the spin 0 Higgs boson and the fundamental fermions quarks and leptons, organized in  $SU(2)_L$  left-handed doublets and  $U(1)_Y$  right handed singlets (see Table 1.1).

Neutrinos are charge-less fermions that can interact only weakly, either via Neutral Current (NC) interactions mediated via  $Z^0$  bosons or charged current via  $W^\pm$  bosons. The flavour of the neutrino is simply defined by the charged lepton that is connected to the same charged current vertex:

$$\begin{aligned} W^+ &\rightarrow e^+ + \nu_e \\ &\rightarrow \mu^+ + \nu_\mu \\ &\rightarrow \tau^+ + \nu_\tau \end{aligned} \tag{1.3}$$

The weak interaction is parity violating and only left-handed particles  $\nu_L$  or right handed anti-particles  $\bar{\nu}_R$  participate to the interaction. For this reason only left-handed neutrino and right-handed neutrino have been introduced in the SM, so making it impossible to construct a Dirac mass term:

$$\mathcal{L}_{\text{mass}}^{\text{Dirac}} = m_D (\bar{\psi}_L \psi_R + \bar{\psi}_R \psi_L), \text{ with } \bar{\psi}_R \psi_L = (\bar{\psi}_L \psi_R)^\dagger \tag{1.4}$$

where  $\psi_{L,(R)}$  is the left(right)-handed chiral component (Weyl spinors). It is obvious then that both a left-handed and a right-handed Dirac neutrino would have to exist for the mass term not to be null. Neutrino flavour oscillations, as we will discuss more in detail later (see Sec. 1.3), require neutrinos to be massive particles.

One solution to this problem is to extend the Standard Model to include a right-handed neutrino  $\nu_R$  [9]. Since neutrinos are neutral, another possibility is that they are Majorana particles, i.e. neutrino and antineutrino are the

same particle. Such a fermion would be described by a single Weyl spinor. A Majorana mass term with a single Weyl-spinor, either left or right handed can then be introduced as:

$$\mathcal{L}_{mass}^{Majorana} = -\frac{m_M}{2}[(\psi_L)^T i\sigma^2 \psi_L + h.c.]. \quad (1.5)$$

In principle it is possible to construct both a Dirac and a Majorana term. This could be written as:

$$\mathcal{L}_{mass}^\nu = -\frac{1}{2}(\bar{\psi}_L, \bar{\psi}_L^c) \begin{pmatrix} m_{M,L} & m_D \\ m_D & m_{M,R} \end{pmatrix} \begin{pmatrix} \psi_R^c \\ \psi_R \end{pmatrix} \quad (1.6)$$

where c stands for the the conjugation operation. The Dirac mass term can be expected to be about the same as for the other fermions in the family while the Majorana mass term  $m_{M,L}$  should be null to not break  $SU(2)_L \times U(1)_Y$  symmetry ( $m_{M,L} \gg m_D$ ). Finally a right handed neutrino would be completely neutral under the standard-model gauge-group (i.e *sterile*), and it could have a mass above the symmetry breaking scale ( $v = 246$  GeV), without actually breaking any symmetry. The mass  $m_{M,R}$  could then be associated to a different higher mass scale  $M$ :

$$\mathcal{M} \simeq \begin{pmatrix} 0 & m_D \\ m_D & M \end{pmatrix} \quad (1.7)$$

This matrix can be diagonalized to obtain two eigenvalues that are approximatlly  $M$  and  $-m_D^2/M$ . The two mass eigenvalues correspond to one very massive and sterile ( $m_N \simeq M$ ) and one very light and weakly interacting ( $m_\nu \simeq m_D^2/M$ ). The second particle would correspond to the neutrinos we normally observe. This so-called *see-saw* mechanism is one of the possible explanations for the smallness of the neutrino masses.

The main experimental technique used today to confirm whether neutrinos are Majorana particles or more canonical Dirac fermions is the search for the so called neutrino-less double beta decay, a process only possible if neutrinos and antineutrinos are the same particle. Some of the experiments now active in the field now include Gerda, CUORE and CuPID and CANDLES [10].

### 1.2.1 Limits on neutrino masses

While the existence of the neutrino oscillation phenomenon is an indicator of the fact that neutrinos must have a mass, it depends only on the squared mass differences and as such, they can't be used to obtain limits on the mass values. A direct measurement of neutrino masses is possible, in principle,

using kinematical methods, though these strategies have only produced upper limits so far.

For  $\bar{\nu}_e$  the most effective technique relies on the measurement of the highest kinematically allowed energy in the  $\beta$ -decay spectrum. Such value is related to the neutrino mass as :  $E_{\text{endpoint}}^e \simeq Q - m_\nu$ . The best limit is currently set by the KATRIN experiment [13], which has recently halved the previous estimates from the Troitsk [11] and Mainz [12] experiments (all study the decay of tritium):

$$\begin{aligned} m_{\nu_e} &< 2.05 \text{ eV at 95\% C.L. (Troitsk)}; \\ &< 2.3 \text{ eV at 95\% C.L. (Mainz)}; \\ &< 1.1 \text{ eV at 90\% C.L. (KATRIN)}; \end{aligned} \quad (1.8)$$

Limits on the masses of the other flavours [14] are currently much less stringent and are obtained by studying the pion decay and the  $\tau$  decay kinematics for  $\nu_\mu$  and  $\nu_\tau$  respectively:

$$\begin{aligned} m_{\nu_\mu} &< 170 \text{ keV at 90\% C.L.}; \\ m_{\nu_\tau} &< 18.2 \text{ MeV at 95\% C.L.}; \end{aligned} \quad (1.9)$$

Limits on the sum of the three masses can also be set by cosmological experiments such as Planck. These limits are model dependent and in the Standard Cosmological Model are currently set at:

$$\sum_j m_j \leq 0.12 \text{ eV} \quad (1.10)$$

Finally the non observation of neutrino-less double beta decay can set a limit on the electron neutrino effective mass in the case that neutrinos are Majorana particles:

$$\langle m_{\nu_e} \rangle_{\text{eff}} \lesssim 0.4 \text{ eV} \quad (1.11)$$

### 1.3 Theory of neutrino oscillations

If neutrinos have non-vanishing rest mass, the weak and mass eigenstates are not necessarily the same, a fact that is well known in the quark sector where the CKM matrix connects the two types of states. This makes the phenomenon of neutrino oscillations possible i.e. a neutrino produced with a specific flavour can later be measured to have a different flavour. The experimental discovery of this new behaviour in 1998 is currently the unique evidence that the Standard Model is not a complete theory. [15] [16]

### 1.3.1 Three flavours oscillations in vacuum

The 3 orthonormal flavour eigenstates  $|\nu_\alpha\rangle$  (where  $\alpha = e, \mu, \tau$ ) are connected to 3 orthonormal mass eigenstates  $|\nu_i\rangle$  via a unitary mixing matrix  $U$  [15]:

$$|\nu_\alpha\rangle = \sum_i U_{\alpha i} |\nu_i\rangle ; \quad |\nu_i\rangle = \sum_\alpha U_{\alpha i}^* |\nu_\alpha\rangle ; \quad (1.12)$$

The matrix, in the case of 3 neutrino flavours is the so called PMNS (Pontecorvo-Maki-Nakagawa-Sakata) matrix and can be written as:

$$\begin{aligned} U &= \begin{bmatrix} 1 & 0 & 0 \\ 0 & c_{23} & s_{23} \\ 0 & -s_{23} & c_{23} \end{bmatrix} \begin{bmatrix} c_{13} & 0 & s_{13}e^{-i\delta} \\ 0 & 1 & 0 \\ -s_{13}e^{i\delta} & 0 & c_{13} \end{bmatrix} \begin{bmatrix} c_{12} & s_{12} & 0 \\ -s_{12} & c_{12} & 0 \\ 0 & 0 & 1 \end{bmatrix} = \\ &= \begin{bmatrix} c_{12}c_{13} & s_{12}c_{13} & s_{13}e^{-i\delta} \\ -s_{12} - c_{12}s_{23}s_{13}e^{i\delta} & c_{12}c_{23} - s_{12}s_{23}s_{13}e^{i\delta} & s_{23}c_{13} \\ s_{12}s_{23} - c_{12}c_{23}s_{13}e^{i\delta} & -c_{12}s_{23} - s_{12}c_{23}s_{13}e^{i\delta} & c_{23}c_{13} \end{bmatrix} \end{aligned} \quad (1.13)$$

where  $c_{ij} = \cos \theta_{ij}$ ,  $s_{ij} = \sin \theta_{ij}$ ,  $\theta_{ij}$  are the mixing angles and  $\delta$  is the Dirac charge-parity (CP) symmetry violating phase. In the case of Majorana neutrinos the matrix contains two additional Majorana phases which appear in a diagonal matrix that multiplies  $U$ :

$$U^{Majorana} = \begin{bmatrix} 1 & 0 & 0 \\ 0 & e^{i\phi_2/2} & 0 \\ 0 & 0 & e^{i\phi_3/2} \end{bmatrix} \quad (1.14)$$

These additional phases do not affect neutrino oscillations and cannot be measured in neutrino oscillation experiments.

The mass eigenstates  $|\nu_i\rangle$ , being the eigenstates of the Hamiltonian ( $\mathcal{H}|\nu_i\rangle = E_i|\nu_i\rangle$ ) show a time dependence :

$$|\nu_i(t)\rangle = e^{-iE_it} |\nu_i\rangle \quad (1.15)$$

with  $E_i = \sqrt{\vec{p}^2 + m_i^2}$  in natural units (i.e.  $c = 1$ ). If we now consider a flavour state  $|\nu_\alpha(t)\rangle$  which represents a neutrino of definite flavour created at  $t=0$  ( $|\nu_\alpha(t=0)\rangle = |\nu_\alpha\rangle$ ), from eq. 1.12 and 1.15 the time evolution of this state is given by:

$$\begin{aligned} |\nu_\alpha(t)\rangle &= \sum_i U_{\alpha i} e^{-iE_it} |\nu_i\rangle \\ &= \sum_\beta \left( \sum_i U_{\alpha i}^* e^{-iE_it} U_{\beta i} \right) |\nu_\beta\rangle \end{aligned} \quad (1.16)$$

The amplitude of the transition  $\nu_\alpha \rightarrow \nu_\beta$  is then:

$$\mathcal{A}_{\nu_\alpha \rightarrow \nu_\beta}(t) = \langle \nu_\beta | \nu_\alpha(t) \rangle = \sum_i U_{\alpha i}^* U_{\beta k} e^{-i E_i t} \quad (1.17)$$

The transition probability is given by the square of the modulus of the amplitude:

$$P_{\nu_\alpha \rightarrow \nu_\beta}(t) = |\mathcal{A}_{\nu_\alpha \rightarrow \nu_\beta}(t)|^2 = \sum_{i,j} U_{\alpha i}^* U_{\beta i} U_{\alpha j} U_{\beta j}^* e^{-i(E_i - E_j)t} \quad (1.18)$$

Due to their tiny masses, neutrinos are always ultra-relativistic ( $p \gg m$ ) we can approximate:

$$E_i = \sqrt{p^2 + m_i^2} \simeq p + \frac{m_i^2}{2p} \simeq E + \frac{m_i^2}{2E}; \quad t \simeq L; \quad (1.19)$$

with  $L$  being the distance travelled by the neutrino. The probability then can be written as:

$$P_{\nu_\alpha \rightarrow \nu_\beta}(L, E) = \sum_{i,j} U_{\alpha i}^* U_{\beta i} U_{\alpha j} U_{\beta j}^* \exp\left(-i \frac{\Delta m_{ij}^2 L}{2E}\right) \quad (1.20)$$

where  $\Delta m_{ij}^2 = m_i^2 - m_j^2$ . The oscillation probability is then dependent on the difference between the squared mass eigenvalues  $\Delta m_{32}^2$  and  $\Delta m_{21}^2$ , called atmospheric and solar squared mass difference respectively, the three mixing angles  $\theta_{ij}$  and the Dirac CP violation phase  $\delta$ . It also depends on the  $L/E$  ratio, which is one of the main features defining the different types of neutrino oscillation experiments.

Concerning neutrino mass eigenvalues two scenarios are possible: the so-called *normal* and *inverted ordering*. In normal ordering, neutrino mass eigenvalues are ordered  $m_1 < m_2 < m_3$ , while in inverted ordering  $m_3 < m_1 < m_2$  (Fig. 1.2).

### 1.3.2 Charge-parity symmetry violation

Since all mixing angles are not null, if the Dirac phase  $\delta$  is different from 0 or  $\pi$ , neutrino oscillations are CP violating phenomena. CP violation is manifested if the oscillation probability of  $\nu_\alpha \rightarrow \nu_\beta$  are different from the CP conjugate  $\bar{\nu}_\alpha \rightarrow \bar{\nu}_\beta$ . An observable for such effects would then be the CP asymmetry:

$$\mathcal{A}_{\alpha\beta}^{CP} = P(\nu_\alpha \rightarrow \nu_\beta) - P(\bar{\nu}_\alpha \rightarrow \bar{\nu}_\beta); \quad \alpha \neq \beta \text{ and } \alpha, \beta = e, \nu, \tau \quad (1.21)$$

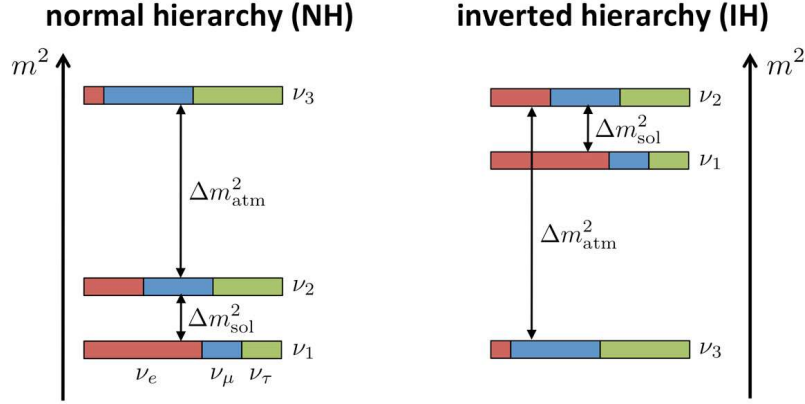


Figure 1.2: Neutrino mass eigenstates possible orderings in normal (left) and inverted (right) hierarchy. The flavour composition of the three states is shown by dividing the bars into colors: red for  $\nu_e$  blue for  $\nu_\mu$  and green for  $\nu_\tau$ . [16]

As a consequence of the CPT theorem a CP asymmetry would imply a T asymmetry offering a second observable:

$$\mathcal{A}_{\alpha\beta}^T = P(\nu_\alpha \rightarrow \nu_\beta) - P(\nu_\beta \rightarrow \nu_\alpha); \quad \alpha \neq \beta \text{ and } \alpha, \beta = e, \nu, \tau \quad (1.22)$$

In the three neutrino mixing case the magnitude of the CP violation is determined by the so-called Jarlskog invariant  $J^{CP}$  in direct analogy with the quark sector:

$$\mathcal{A}_{\alpha\beta}^{CP} = -16 J_{\alpha\beta}^{CP} \sin\left(\frac{\Delta m_{12}^2}{4E} L\right) \sin\left(\frac{\Delta m_{23}^2}{4E} L\right) \sin\left(\frac{\Delta m_{13}^2}{4E} L\right) \quad (1.23)$$

$$\text{with } J^{CP} = Im[U_{\alpha 1} U_{\alpha 2}^* U_{\beta 1}^* U_{\beta 2}] = \pm c_{12} s_{12} c_{23} s_{23} c_{13}^2 s_{13} \sin \delta$$

Current constraints for the mixing angles imply that the value of  $J_{\alpha\beta}^{CP}$  should be in the range:

$$0.026 |\sin \delta| \lesssim |J_{\alpha\beta}^{CP}| \lesssim 0.036 |\sin \delta| \quad (1.24)$$

The asymmetry observable can be approximated in the three-flavour case as [42]:

$$\mathcal{A}_{CP} \simeq \frac{\cos \theta_{23} \sin 2\theta_{12}}{\sin \theta_{23} \sin \theta_{13}} \left( \frac{\Delta m_{21}^2 L}{4E_\nu} \right) \sin \delta_{CP} + \text{matter effects} \quad (1.25)$$

### 1.3.3 Two flavor scenario

Since most experiments are sensitive to oscillations that are driven by a single squared mass difference, an important approximation of the neutrino oscillation phenomenon is the special case in which only two flavours are considered.

In this simplified case the mixing matrix is two dimensional and depends only on one mixing angle. In the case of  $\nu_e$  and  $\nu_\mu$  we get:

$$\begin{pmatrix} \nu_e \\ \nu_\mu \end{pmatrix} = \begin{pmatrix} \cos \theta & \sin \theta \\ -\sin \theta & \cos \theta \end{pmatrix} \begin{pmatrix} \nu_1 \\ \nu_2 \end{pmatrix} \quad (1.26)$$

The two-flavour transition probability ,using the formulas from the previous section then becomes:

$$P(\nu_e \rightarrow \nu_\mu) = \sin^2 2\theta \times \sin^2 \left( \frac{\Delta m^2 L}{4E} \right) \quad (1.27)$$

Since no CP symmetry violation is possible the probability is the same for  $\nu_\mu \rightarrow \nu_e$  and for  $\bar{\nu}_\mu \rightarrow \bar{\nu}_e$ .

The *survival* probability of the particle not changing flavour is simply .

$$P(\nu_e \rightarrow \nu_e) = 1 - P(\nu_e \rightarrow \nu_\mu) \quad (1.28)$$

The oscillatory term can also be rewritten as:

$$\sin^2 \left( \frac{\Delta m^2 L}{4E} \right) = \sin^2 \left( \frac{L}{L_0} \right) \quad (1.29)$$

with  $L_0 = 4 \frac{E}{\Delta m^2}$

where  $L_0$  is the oscillation length and describes the period of one full oscillation cycle. It is proportional to  $E$ , and inversely proportional to  $\Delta m^2$ . The oscillation probability will then be maximum for  $L/L_0 = 1/2$  and its amplitude will be given by  $\sin^2 \theta$  (Fig. 1.3).

### 1.3.4 MSW matter effects

When neutrinos travel through matter, they can coherently interact with electrons and nuclei in the medium and their oscillation probability is modified as it was first noticed by Mikhaev, Smirnov and Wolfenstein, from which the MSW effect takes its name [17].

The MSW effect has origin from the fact that  $\nu_e$  and  $\bar{\nu}_e$  are the only neutrino

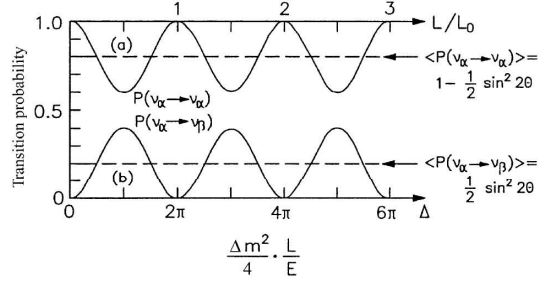


Figure 1.3: Two flavour oscillation probability as a function of  $L/L_0$ , where  $L_0 = 4E/\Delta m^2$ : disappearance  $P(\nu_\alpha \rightarrow \nu_\alpha)$  (upper curve); appearance  $P(\nu_\alpha \rightarrow \nu_\beta)$  (bottom curve) [15]

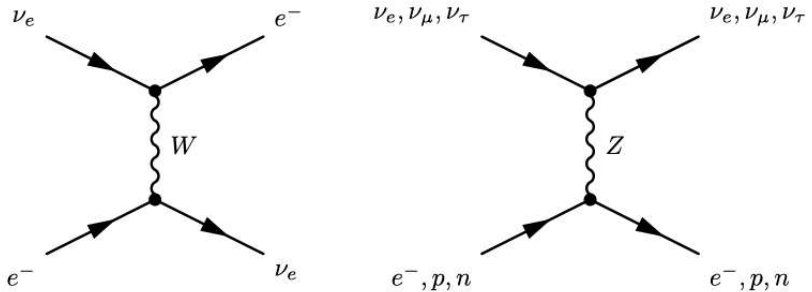


Figure 1.4: Feynmann diagram of CC electronic neutrino interactions  $\nu_e + e^- \rightarrow \nu_e + e^-$  (left) and of NC neutrino interactions  $\nu_\alpha + e^- \rightarrow \nu_\alpha + e^-$  (right)

flavour that can take part both in charged current interactions, and NC elastic interactions with electrons, while  $\nu_\mu$  and  $\nu_\tau$  can only have NC interactions with electrons. This introduces an extra potential in the hamiltonian of the electron neutrinos:

$$V_e = \pm \sqrt{2} G_F N_e \quad (1.30)$$

where  $N_e$  is the electron number density in the medium,  $G_F$  is the Fermi constant and the sign is positive for neutrinos and negative for antineutrinos.

Using a simplified two flavour approach [18] the effective Hamiltonian of neutrino propagation in matter ( $\mathcal{H}_M$ ) then gains an extra  $\nu_e - \nu_e$  element with respect to the Hamiltonian in vacuum ( $\mathcal{H}$ ) and becomes:

$$\mathcal{H}_M = \mathcal{H} + \begin{pmatrix} V_e & 0 \\ 0 & 0 \end{pmatrix} = \left( \frac{\Delta m^2}{4E} \right) \begin{pmatrix} -\cos 2\theta & \sin 2\theta \\ \sin 2\theta & \cos 2\theta \end{pmatrix} + \begin{pmatrix} V_e & 0 \\ 0 & 0 \end{pmatrix} \quad (1.31)$$

In the simple case where the matter density is constant, we can then re-diagonalise  $\mathcal{H}_M$  to obtain a new mixing matrix and mass eigenstates. We can then denote the new effective parameters as  $\theta_M$  and  $\Delta m_M^2$  and the oscillation

probability takes the usual form:

$$P(\nu_e \rightarrow \nu_\mu) = \sin^2 2\theta_M \sin^2 \left( \frac{\Delta m_M^2 L}{4E} \right) \quad (1.32)$$

The new parameters then become:

$$\begin{aligned} \Delta m_M^2 &= M \Delta m^2 \\ \sin 2\theta_m &= \frac{\sin 2\theta}{M} \end{aligned} \quad (1.33)$$

with coefficient  $M$  being:

$$M = \sqrt{\left( \cos 2\theta - \hat{A} \right)^2 + \sin^2 2\theta} \quad (1.34)$$

and:

$$\hat{A} = \pm \frac{2\sqrt{2}G_F N_e E}{\Delta m^2} \quad (1.35)$$

Matter effects have some very crucial consequences in the field of neutrino oscillation:

1. Either long travel distances or high matter densities are necessary in order for the MSW effects to be appreciable (if  $\Delta m_M^2 L / 4E \ll 1$  we return to vacuum probabilities)
  2. There is a resonant condition for which the oscillation probability is significantly enhanced with respect to the one in vacuum. That is when:
- $\hat{A} = \cos 2\theta \quad (1.36)$
3. Oscillation probabilities can be different for neutrinos and antineutrinos even if there is no CP violation, due to the  $\pm$  sign in the effective potential  $V_e$ .
  4. The resonant condition can be met only if  $\hat{A} > 0$ , which depends on the sign of the squared mass difference  $\Delta m^2$ . This fact makes matter effects an effective probe to study mass ordering. In particular it can be studied in long baseline accelerator experiments which are sensitive to muon-electron neutrino oscillation.

## 1.4 Neutrino oscillation experiments

The first subdivision between different neutrino oscillation experiments is determined by what the experiment is trying to measure [16]:

- **Appearance experiments:** These experiments look for signals from neutrino flavours that are not present in the initial composition of the flux.
- **Disappearance experiments:** These experiments measure the number of signals from the various flavours of neutrinos and confront it with the expected one in order to compute the survival probability.

The second distinction is between the different sources of neutrinos. The most important ones are:

- **Reactor experiments:** they use large fluxes of  $\bar{\nu}_e$  produced by beta decays of fission fragments in nuclear power plants;
- **Accelerator experiments:** they use beams of neutrinos produced in decays of secondary mesons (mainly  $\pi$  and  $K$ ), generated by a proton beam hitting a target;
- **Atmospheric neutrino experiments:** they detect neutrinos produced in the decays of mesons originated from the interactions of cosmic rays with nuclei in the atmosphere;
- **Solar neutrino experiments:** they detect neutrinos generated in thermonuclear reactions in the core of the Sun;

This distinction is important not only because of the very different experimental setups, but also because the neutrino source and where the detectors are located with respect to it, determine the constants of nature to which the experiments are sensitive. Specifically experiments can be sorted according to the value of  $\Delta m^2$  to which they are sensitive. The condition for an experiment to be sensitive to a specific mass squared difference is that:

$$\frac{\Delta m^2 L}{2E} \sim 1 \quad (1.37)$$

If this value is too small the oscillation simply does not occur, if it is too large only the average transition probability is measurable and no information on  $\Delta m^2$  can be obtained. The different experiments are then classified depending on the ratio  $L/E$ , which determines the sensitivity:

- **Short Base-Line (SBL):** These are either reactor or accelerator experiments. In the first case the experiments measure the survival probability and are active in the  $L/E$  range:

$$\frac{L}{E} \lesssim 10\text{m}/\text{MeV} \implies \Delta m^2 \gtrsim 1\text{eV}^2 \quad (1.38)$$

- **Long Base-Line (LBN):** these experiments have sources similar to SBL ones but have a distance between source and detector that is 10 or 100 times larger:

$$\begin{aligned} \frac{L}{E} \lesssim 10^3\text{km}/\text{GeV} &\implies \Delta m^2 \gtrsim 1\text{eV}^2 \text{ (Accelerator)} \\ \frac{L}{E} \lesssim 10^3\text{m}/\text{MeV} &\implies \Delta m^2 \gtrsim 1\text{eV}^2 \text{ (Reactor)} \end{aligned} \quad (1.39)$$

In this category are also included the Atmospheric neutrino experiments:

$$\frac{L}{E} \lesssim 10^4\text{km}/\text{GeV} \implies \Delta m^2 \gtrsim 1\text{eV}^2 \text{ (ATM)} \quad (1.40)$$

- **Very Long Base-Line (VLB):** these experiments have a distance between source and detector that is 10 or 100 times larger than for LBN experiments:

$$\begin{aligned} \frac{L}{E} \lesssim 10^5\text{m}/\text{MeV} &\implies \Delta m^2 \gtrsim 10^{-5}\text{eV}^2 \text{ (Reactor)} \\ \frac{L}{E} \lesssim 10^4\text{km}/\text{GeV} &\implies \Delta m^2 \gtrsim 10^{-4}\text{eV}^2 \text{ (Accelerator)} \end{aligned} \quad (1.41)$$

In this category are also included the Solar neutrino experiments:

$$\frac{L}{E} \lesssim 10^{12}\text{m}/\text{MeV} \implies \Delta m^2 \gtrsim 10^{-12}\text{eV}^2 \text{ (Sol)} \quad (1.42)$$

#### 1.4.1 Solar experiments: $\theta_{12}$ and $\Delta m_{12}^2$

The Sun produces an intense flux of neutrinos as a sub-product of some of the thermonuclear reactions that produce energy in its interior by burning hydrogen into helium [19]. There are two main cycles of reactions that can produce neutrinos: the pp cycle and CNO (Carbon-Nitrogen-Oxygen) cycle. Both can be summarized as:



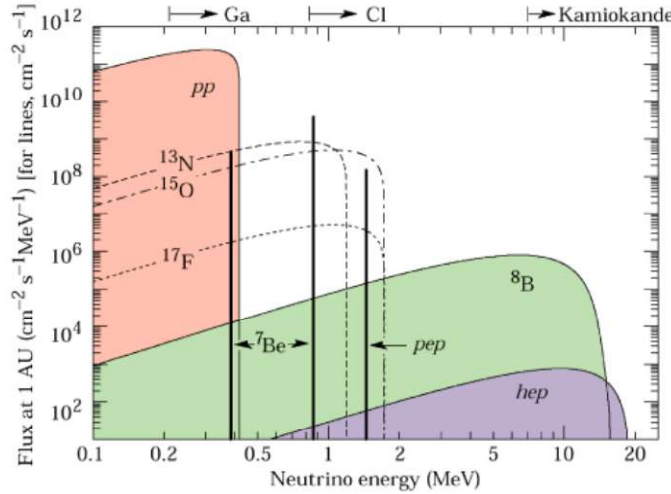


Figure 1.5: Spectrum of solar neutrinos, modelled from the SSM. The arrows indicate the sensitivity range of some of the experiments [19]

The expected flux of  $\nu_e$ , can be computed using the standard solar model (SSM), which is a detailed mathematical model of the reactions taking place in the solar interior (Fig. 1.5).

The solar neutrino experiments can be divided into two main categories depending on the revelation techniques: radiochemical and Cherenkov. In the first field we find experiments such as Homestake, Gallex/GNO and Sage [20] [21] [22]. These experiments exploit the Inverse Beta Decay (IBD) reaction of solar neutrino with  $^{37}\text{Cl}$ ,  $^{71}\text{Ga}$  and  $^{71}\text{Ge}$  respectively). These have a relatively low energy threshold ( $E_\nu \gtrsim 0.23 - 0.81$  MeV), but they are not able to give any information on direction, energy or time of the event.

The Cherenkov technique was pioneered by the Kamiokande experiment [23], consisting of a tank of about 3000 tons of pure water and 1000 photomultipliers positioned on the inner walls. The experiment observed the Cherenkov light produced by recoil electrons in elastic scattering interactions of  $\nu_e$  with  $e^-$ , which have an energy threshold of  $E \gtrsim 5\text{MeV}$ :

$$(ES) \quad \nu_e + e^- \rightarrow \nu_e + e^- \quad E \gtrsim 5\text{MeV} \quad (1.44)$$

This technique was capable of measuring neutrino interactions in real time while also giving informations on direction and energy. This capability was crucial in confirming the existence of the so called *solar neutrino problem*, a deficit in the number of neutrinos arriving from the Sun between 1/2 and 2/3 with respects to the predictions of the SSM, measured by the earlier radiochemical experiments.

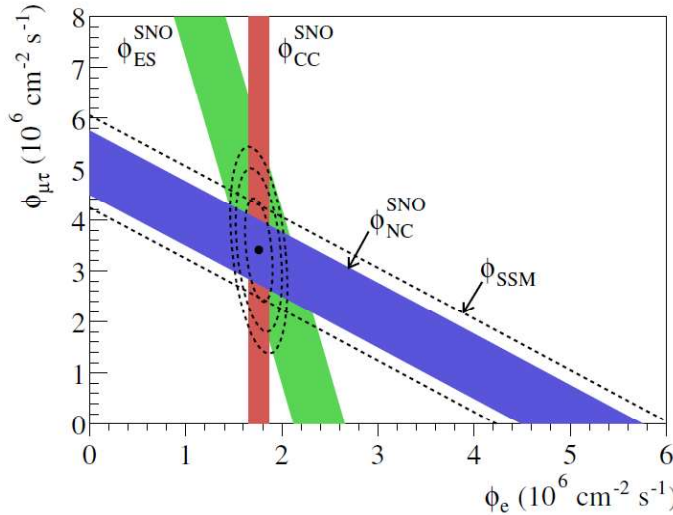


Figure 1.6: Flux of muon and tau neutrinos  $\phi_{\mu\tau}$  over electron neutrino  $\phi_e$  as measured by SNO. The three coloured bands correspond to the three possible interactions: electron scattering ES (green); charged current CC (red); neutral current NC (blue). The dashed band gives the prediction from the SSM which is in agreement with the NC measurements. [24]

The Kamiokande experiment was able to measure the flux of  $\nu_e$ . Differently, the SNO experiment in which, thanks to the use of heavy water ( $d_2O$ ) rather than purified water as target, two more reactions were available for detection [24]:

$$\begin{aligned} (\text{CC}) \quad & \nu_e + d \rightarrow p + p + e^-; \quad E \gtrsim 5\text{MeV} \\ (\text{NC}) \quad & \nu_f + d \rightarrow p + n + \nu_f; \quad f = e, \mu, \tau \quad E \gtrsim 2.2\text{MeV} \end{aligned} \quad (1.45)$$

With the first reaction being sensitive only to  $\nu_e$  while the second is sensitive to all flavours. What SNO found was that the combined tau and mu fluxes were two times more intense than the  $\nu_e$  one and that the total flux was in agreement with the predictions from the SSM (Fig. 1.6).

The characteristic L/E for the solar experiments are of the VLB range, making them sensitive to the  $\Delta m_{12}^2$  squared mass difference and to  $\sin 2\theta_{12}$ . For this reason the two parameters are often referred to as solar mass difference and solar mixing angle ( $\Delta m_{\odot}^2, \theta_{\odot}$ ). As already noted these two parameters can be measured also by VLB reactor experiments such as KamLand [25] (discussed in Sec.1.4.2). The most precise values for the parameters are obtained combining the results from both (Fig. 1.7).

Other important and more recent Solar experiments include Borexino [26],

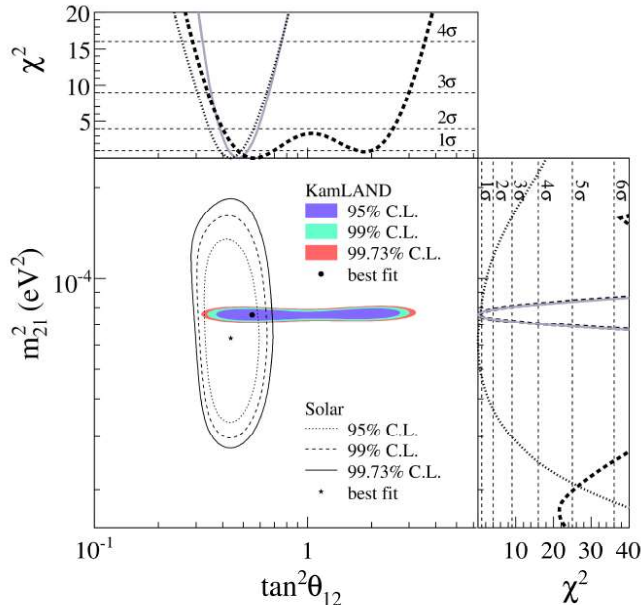


Figure 1.7: Confidence level intervals for the solar oscillation parameters from KamLAND and the combined results from solar experiments. The side-panels show the respective  $\chi^2$  profiles: KamLAND (dashed); solar experiments (dotted) individually; combined (solid) [25]

which was the first with an energy threshold low enough to measure the monochromatic flux of  ${}^7Be$  and *pep* neutrinos and Super-K, the successor of Kamiokande. The results from both experiments are in agreement with the neutrino oscillation hypothesis.

### 1.4.2 Reactor experiments

#### VLB: confirmation of solar experiment results

Neutrinos from nuclear reactors are  $\bar{\nu}_e$  with energy of the order of the MeV. This makes the particles above threshold for electronic CC interactions, but not for other flavours, which means that if the neutrino oscillates CC interactions cannot happen. Reactor experiments can then measure the disappearance probability of the  $\bar{\nu}_e$  and they are usually sensitive to small values of  $\Delta m^2$  due to the low energy spectrum of the neutrinos.

Very Long Baseline experiments proved to be sensitive to the solar square mass difference and were able to give confirmation on the Solar experiment results, while at the same time improving the sensitivity to the parameter and beginning the precision era of neutrino physics.

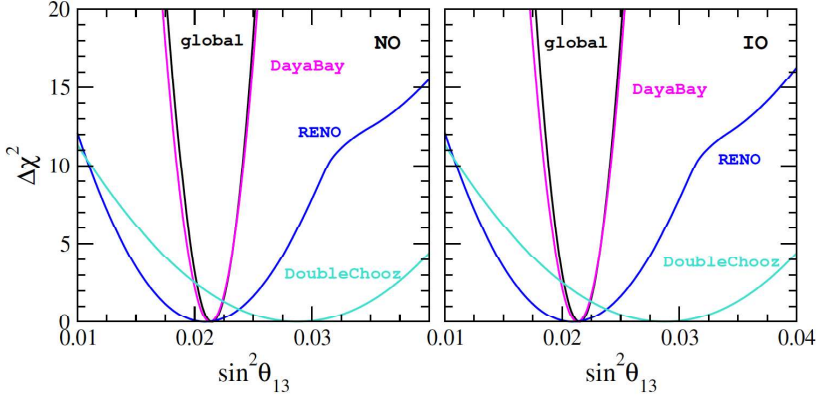


Figure 1.8:  $\chi^2$  profile as a function of  $\sin \theta_{13}$  for RENO DataBay and Double Chooz and the combined result (black line). The results are fitted for normal ordering (left) and inverse ordering (right) [31]

In particular the KamLAND experiment, located in the Kamioka mines in Japan , was the first to give independent confirmation of the results from the solar neutrino sector. It consists of a 1000 ton liquid scintillator detector measuring the interactions of  $\bar{\nu}_e$  from a cluster of nuclear reactors located at an average distance of  $L \simeq 175$  km. The antineutrinos interact via inverse beta decay at an energy threshold of  $E > 2.6$  MeV:

$$\bar{\nu}_e + p \rightarrow e^+ + n \quad E > 2.7 \text{ MeV} \quad (1.46)$$

The experiment exploited the signature given by the  $e^+$  annihilation and the delayed neutron thermalisation and capture proved very effective in the reduction of background. This level of precision was also crucial in excluding alternative explanations for neutrino oscillations based on exotic interactions or magnetic transition moments [27].

### Measurement of $\theta_{13}$

Recently Short Baseline experiments such as Data Bay [28], RENO [29] and Double Chooz [30] have been able to measure the disappearance of reactor electron antineutrinos at distances  $L \sim 1$  km. Their characteristics made them sensitive to the measurement of the  $\theta_{13}$  mixing angle.

Compared to previous experiments such as CHOOZ and Palooverde, these have not only access to larger statistics, thanks to the increased reactor power and larger detectors, but they also have access to multiple detectors at different distances from the reactor core. Measurements at the closest detectors can then be utilized to more accurately predict the expected number of

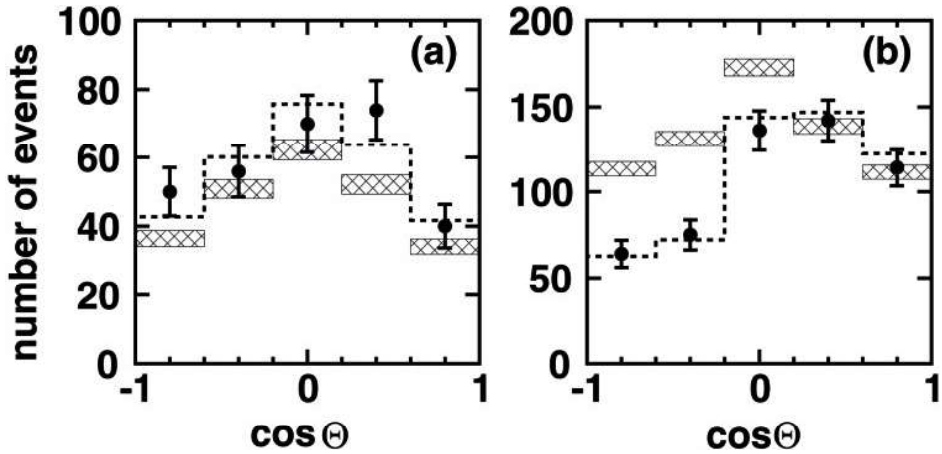


Figure 1.9: Zenith angle  $\Theta$  distributions for the most energetic multi-GeV atmospheric neutrino events measured by Super-Kamiokande over a 535 days period. Filled histograms are the Monte Carlo predictions and dotted histograms are the experimental measurements. Right and left panels are  $\mu$ -like and  $e$ -like events respectively. [32]

events at the more distant ones.

The combined results from the experiments are shown in Fig. 1.8

### 1.4.3 Atmospheric experiments: $\Delta m_{31}^2$ and $\theta_{23}$

The cosmic ray interactions with the atmosphere nitrogen and oxygen nuclei produce mostly pion and kaons that decay in electron and muon neutrino as well as antineutrinos.  $\nu_e$  decay from the chain :  $\pi \rightarrow \mu\nu_\mu$  followed by  $\mu \rightarrow e\nu_\mu\nu_e$ . One then would expect the ratio to be of the order:

$$R = \frac{N(\nu_\mu + \bar{\nu}_\mu)}{N(\nu_e + \bar{\nu}_e)} \sim 2 \quad (1.47)$$

Experiments originally built to look for proton decay in the '70s and '80s, which had atmospheric neutrinos as background, were the first to observe a deficit of the muon neutrino flux with respect to the Monte Carlo expectations, measured originally as the ratio :  $R_{\mu/e}/R_{\mu/e}^{MC}$ . Two main categories of detectors were in operation: water Cherenkov tanks such as Super Kamiokande [32] and iron calorimeters such as Soudan2 [33] and Macro [34]. The first kind of detectors are constituted of tanks filled with water of the order of 1 ton, and they detect the Cherenkov light rings produced by the charged lepton produced in the neutrinoCC interaction using photo multipliers placed on the inside of the walls. Iron calorimeters are instead constituted

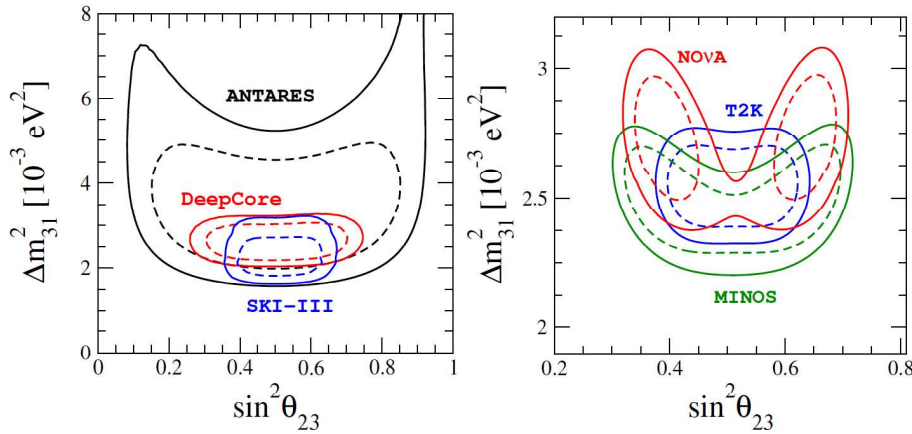


Figure 1.10: 90% CL (straight line) and 99% C.L.(dashed line) regions in the atmospheric parameter plane ( $\Delta m_{31}^2$  over  $\sin^2 \theta_{23}$  from atmospheric (left) and long baseline accelerator (right) experiments, assuming normal mass hierarchy. [31]

of layers of iron, acting as a passive materials and active layers, made for example of plastic scintillators, which track either the electromagnetic showers produced by  $e^\pm$  or long muon tracks. Both techniques are capable of flavour identification and direction and energy estimation.

In 1998 the Super-Kamiokande was among the first to observe the anomalous deficit. The experiment distinguished between muon and electron neutrino events, measured the lepton zenith angle with respect to the Earth's axis (correlated to that of the parent neutrino direction) and divided the samples differentiating according to the lepton energy (the more energetic events having a stronger direction dependency with that of the parent neutrino). These measurements made it possible to observe the variation of the flux as a function of the energy and zenith angle and thus the  $L/E$  travelled by the parent neutrino (Fig. 1.9).

Super-Kamiokande showed that while the electron events had no reduction, the muon events had a deficit of almost 50% for up-going neutrinos ( $\cos \Theta = -1$ ). The results can be explained considering as due to the neutrino oscillation phenomena driven by the parameters  $\Delta m_{23}^2$  and  $\theta_{23}$  that for this reason are often referred to as atmospheric oscillation parameters :  $\Delta m_{ATM}^2$ ,  $\theta_{ATM}$ . The best fit values for these parameters are today given by combining the results of Super-Kamiokande with the ones from modern neutrino telescopes ANTARES and IceCube (Fig. 1.10).

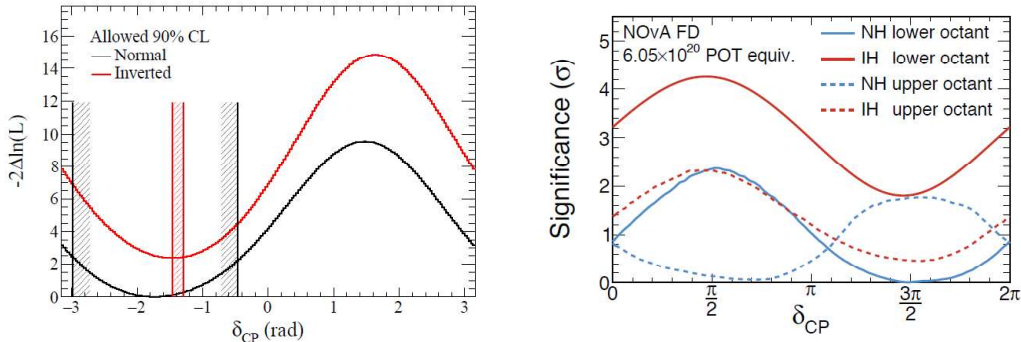


Figure 1.11: (Left) Log-likelihood function of  $\delta_{CP}$  with 90% CL for normal (black) and inverted (red) hierarchy at T2K (Right) Significance as function of  $\delta_{CP}$  at NO $\nu$ A in all combinations of mass ordering and  $\theta_{23}$  octant [43]

#### 1.4.4 Accelerator experiments

The first two experiments to confirm the atmospheric oscillation results were K2K (KEK to Kamioka) in Japan and MINOS at Fermilab. K2K used a beam of about 98%  $\nu_\mu$  with a mean energy of about 1.3 GeV produced from 12 GeV protons accelerated at the KEK synchrotron. The experiment had a near detector at about 300 m from the proton target, and used Super-Kamiokande as its far detector at about 250 km. The K2K data sample taken from 1999 to 2005 (K2K-I and II) contained about 112 muonic events versus the 158 expected without oscillation, confirming the findings in the atmospheric sector [35]. MINOS also looked for  $\nu_\mu$  disappearance using the NuMi neutrino beam at  $E \sim 3$  GeV. Much like K2K it had a near detector at about 1 km from the source and a second detector in the Soudan mines at about 735 km away as its far detector. The first results published in 2006, combined with the ones from K2K first confirmed neutrino oscillations at  $5\sigma$  [36].

Long Baseline experiments such as OPERA and ICARUS worked instead in the appearance channel looking for signatures of  $\nu_\tau$  in  $\nu_\mu$  beams. The OPERA experiment in particular found 5  $\nu_\tau$  candidates in a sample of  $1.8 \times 10^{19}$  POT (protons on target) from the CNGS beam. This was enough to confirm muon neutrino oscillation at  $5\sigma$  [37]. Short baseline experiments such as NOMAD [38] and CHORUS [39] at CERN also studied the  $\nu_\mu \rightarrow \nu_\tau$  channels but did not observe any oscillations.

Current experiments such as T2K (Tokai to Kamioka) [40], the successor of K2K, and NoVA[41] both use muon neutrino beam and perform precision

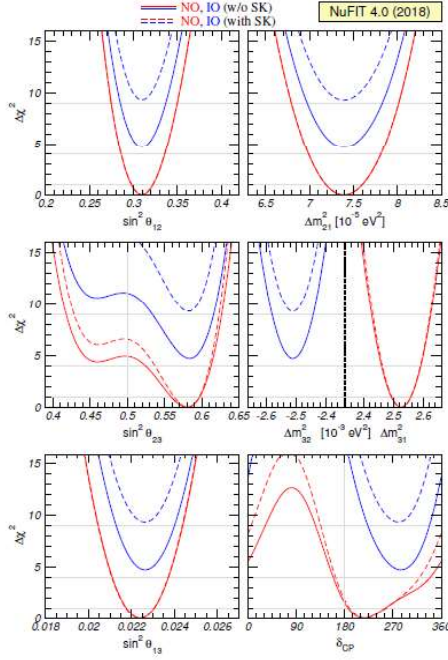


Figure 1.12:  $\Delta\chi^2$  profile obtained from global  $3\nu$  oscillation experiments analysis. The profiles are minimized in all non displayed parameters. The red and blue full curves correspond to the analysis results for NO and IO respectively, without considering the atmospheric data from SuperK. The dashed lines are with the inclusion of this data. For atmospheric mass squared difference  $\Delta m_{31}^2$  is used for NO and  $\Delta m_{32}^2$  for IO. [44]

measurements in both appearance and disappearance channels. Allowed CL areas for the atmospheric parameters  $\Delta m_{31}^2$  and  $\sin^2 \theta_{23}$  obtained from T2K, NoVa and MINOS data can are shown in Fig. 1.10.

#### 1.4.5 $\delta_{CP}$ experimental results

The latest measurements of  $\delta_{CP}$  are from T2K [43]. The experiment measured both the  $\nu_\mu$  survival probability and the  $\nu_e$  appearance probability and then did the same for  $\bar{\nu}_\mu$ . The analysis excludes  $\delta_{CP} = 0^\circ, \pm 180^\circ$  at 90% CL for both mass orderings.

Similar measurements have been performed by the NO $\nu$ A experiment. The analysis found two best-fit points for normal mass ordering :  $\sin^2 \theta_{23} = 0.404$   $\delta_{CP} = 1.48\pi$  and  $\sin^2 \theta_{23} = 0.623$   $\delta_{CP} = 0.74\pi$ . It also found that the inverted mass ordering is disfavoured at > 93% regardless of the value of the CP phase.

Parameter	Ordering	Best fit	$1\sigma$ range	$2\sigma$ range	$3\sigma$ range
$\delta m^2/10^{-5} \text{ eV}^2$	NO, IO, Any	7.37	7.21 – 7.54	7.07 – 7.73	6.93 – 7.96
$\sin^2 \theta_{12}/10^{-1}$	NO, IO, Any	2.97	2.81 – 3.14	2.65 – 3.34	2.50 – 3.54
$ \Delta m^2 /10^{-3} \text{ eV}^2$	NO	2.525	2.495 – 2.567	2.454 – 2.606	2.411 – 2.646
	IO	2.505	2.473 – 2.539	2.430 – 2.582	2.390 – 2.624
	Any	2.525	2.495 – 2.567	2.454 – 2.606	2.411 – 2.646
$\sin^2 \theta_{13}/10^{-2}$	NO	2.15	2.08 – 2.22	1.99 – 2.31	1.90 – 2.40
	IO	2.16	2.07 – 2.24	1.98 – 2.33	1.90 – 2.42
	Any	2.15	2.08 – 2.22	1.99 – 2.31	1.90 – 2.40
$\sin^2 \theta_{23}/10^{-1}$	NO	4.25	4.10 – 4.46	3.95 – 4.70	3.81 – 6.15
	IO	5.89	4.17 – 4.48 $\oplus$ 5.67 – 6.05	3.99 – 4.83 $\oplus$ 5.33 – 6.21	3.84 – 6.36
	Any	4.25	4.10 – 4.46	3.95 – 4.70 $\oplus$ 5.75 – 6.00	3.81 – 6.26
$\delta/\pi$	NO	1.38	1.18 – 1.61	1.00 – 1.90	0 – 0.17 $\oplus$ 0.76 – 2
	IO	1.31	1.12 – 1.62	0.92 – 1.88	0 – 0.15 $\oplus$ 0.69 – 2
	Any	1.38	1.18 – 1.61	1.00 – 1.90	0 – 0.17 $\oplus$ 0.76 – 2

Figure 1.13: Results of recent  $3\nu$  oscillation parameters global fits. The results are given in terms of best fit and  $n\sigma$  ranges under the IO, NO and any ordering assumptions. Note that here  $\delta m^2 \equiv \Delta m^2_{12}$ ,  $\Delta m^2 = m_3^2 - (m_1^2 + m_2^2)/2$  and  $\delta \equiv \delta_{CP}$  is given in terms of cycle intervals  $\delta/\pi \in [0, 2]$ . [45]

#### 1.4.6 Mass hierarchy experimental results

The most recent global fits performed on the oscillation parameters  $\Delta m^2_{32}$ ,  $\Delta m^2_{31}$ ,  $\delta_{CP}$  and  $\sin^2 \theta_{23}$  from LBL accelerator experiments (NO $\nu$ A, MINOS, T2K), reactor experiments (Data Bay, RENO, Double Chooz) and solar experiments (SNO, SuperK, Borexino) show a growing preference towards standard hierarchy. In particular NO is preferred to IO with  $\Delta\chi^2 = 4.7$  (Fig. 1.12). The indication becomes even stronger when one includes data from the measurements on atmospheric neutrinos for Super-Kamiokande where NO is preferred with  $\Delta\chi^2 = 9.3$  [44].

### 1.5 State of the art and future prospects

Neutrino physics is entering its precision era nonetheless there are still fundamental questions that are yet to be fully answered :

- The determination of the absolute mass of the neutrinos and its origin i.e Majorana or Dirac;
- The measurement of CP asymmetries in the leptonic field;
- The determination of the mass ordering (normal or inverse)

While the first field of research is in the domain of the types of experiments described in Section 1.2.1 and, the latter two are best studied in oscillation

experiments. Such goals will require levels of precision still not achieved and new experiments in all categories (reactor, atmospheric, ecc.).

In the long-baseline accelerator field DUNE (Deep Underground Neutrino Experiment), will be the next-generation flagship neutrino oscillation experiment of the Fermilab national laboratories. Having access to MSW effects and to a neutrino beam capable of producing both  $\nu_\mu$  and  $\bar{\nu}_\mu$  will make it particularly well suited to determine the mass ordering and observe CP violations. This will be discussed more in detail in Chapter 2.



# Chapter 2

## DUNE

The Deep Underground Neutrino Experiment (DUNE) will be a new generation world-leading Long Baseline oscillation experiment. Among its main goals are the precise measurement of the oscillation parameters, the study of matter-antimatter asymmetry and the determination of the neutrino mass ordering. It is conceived around three main components: The NuMi neutrino Beam, which is able to produce an intense and wide muon neutrino and antineutrino band; a fine-grained Near Detector (ND) situated at the Fermi National Accelerator Laboratories (Fermilab, Batavia, Illinois), just downstream of the neutrino source; a massive Liquid Argon Time Projection Chamber (LArTPC) Far Detector (FD) placed 1300 km downstream at the Sanford Underground Research Facility (Lead, South Dakota).

In this chapter we will discuss DUNE’s physics programme (Section 1) as well as the configuration of the neutrino beam and its main detectors (Section 3). KLOE, which is one of DUNE’s Near Detectors and the subject of the simulations performed for this thesis will be discussed more in detail in the next chapter.

### 2.1 DUNE’s scientific program

The scientific objectives of DUNE are categorized into a *primary* and an *ancillary* scientific programme [46]. The latter is further divided into secondary objectives that could be pursued by the experiment just by virtue of how it will be built and additional secondary objectives that may require specific upgrades to the facility.

The *primary* programme is made up by the main measurements that DUNE will be built to perform with unprecedented precision which coincide with the fundamental questions that this experiment will try to answer:

1. **Measurement of the charge-parity violating phase  $\delta_{CP}$  and determination of the mass ordering of the neutrinos** (i.e. the sign of  $\Delta m_{31} = m_3^2 - m_1^2$ ). The study of  $\delta_{CP}$  is particularly important in cosmological models trying to explain the matter-antimatter asymmetry in the universe.
2. **Precision measurements of the  $\nu_\mu \rightarrow \nu_{\mu,e}$  oscillation parameters**: the  $\theta_{13}$  mixing angle; the  $\theta_{23}$  mixing angle and the octant it lies in; the value of the  $|\Delta m_{32}^2|$  mass difference. Precision measurements of these parameters and comparisons with corresponding patterns in the quark sector will further our knowledge of the underlying symmetries in fundamental particle physics.
3. **Search for proton decay in one or more decay modes, improving significantly on previous lifetime limits**. Most Grand Unified Theories (GUTs) make lifetime predictions for nucleons and putting more and more stringent limits will be fundamental in assessing which one of them might be correct.
4. **Detection and measurements of the neutrino flux from a core-collapse supernova**. In particular the time structure and energy spectrum of the neutrino burst would much further our understanding of this astrophysical phenomenon.

The *ancillary* programme consists of objectives that DUNE is not specifically conceived to achieve, but that are nonetheless enabled by the facility's design.:

1. Further accelerator oscillation measurements and search for non-standard interactions beyond the standard model (BSD)
2. Atmospheric neutrino oscillation measurements
3. Measurements of other astrophysical phenomena using moderate energy neutrinos

Finally the *additional secondary* programme includes measurements potentially made possible by future upgrades to the facility such as monitoring of the diffuse supernova flux, solar neutrino and other low energy astrophysical neutrino measurements.

The high granularity and precision required by the *DUNE Near Detector (ND)* will also allow it to have a scientific programme of its own. Its main objective will be to perform all the precision measurements necessary to

achieve the goals of the primary programme. It will also pursue precision studies of the weak interaction, studies of nuclear and nucleon structure and searches for new physics (discussed more in detail in Chapter 3).

### 2.1.1 Sensitivities and systematics

In order to make any precision measurement one should be acutely aware of the systematic uncertainties related to the analysis strategy and the performance of the detector. In a two detectors Long Baseline experiment the  $\nu_\mu$  spectrum measured in the Near Detector  $N_{ND}^{data}(\nu_\mu)$  is propagated to the Far Detector and is used to predict the expected signal of  $\nu_\mu$  and oscillated  $\nu_e$  (and much smaller component of oscillated  $\nu_\tau$ ) i.e.  $N_{FD}^{exp}(\nu_\mu)$  and  $N_{FD}^{exp}(\nu_e)$ . Likewise the  $\nu_e$  measured spectrum in the ND, mostly comprised of electron neutrinos from the beam and misidentified NC $\pi^0$  is used to predict the background at the FD.

The measured neutrino spectrum at the near detector is given by:

$$N_{ND}^{data}(\nu_{\mu,e}) = \Phi_{ND}(\nu_{\mu,e}) \otimes \varepsilon_{ND}(\nu_{\mu,e}) \otimes \sigma_{ND}(\nu_{\mu,e}) \quad (2.1)$$

where  $\Phi_{ND}(\nu_{\mu,e})$  is the beam flux,  $\varepsilon_{ND}(\nu_{\mu,e})$  is the detector's efficiency and  $\sigma_{ND}(\nu_{\mu,e})$  is the neutrino interaction cross section. In order to use such data to predict the signal and background expected at the far detector one needs to take into consideration:

- *Differences in how the neutrino interact*  $\sigma_{FD}/\sigma_{ND}$ . These are null in the case that the target nuclei in the Near and Far Detector are the same. Otherwise the dominating uncertainties in the prediction of  $\nu_e$  in FD from measurement of  $\nu_\mu$  in ND are the ones arising from differences in the electronic and muonic cross sections between the detectors:  $\sigma_{FD}(\nu_e)/\sigma_{ND}(\nu_\mu)$ .
- *Differences in detector efficiencies*  $\varepsilon_{FD}/\varepsilon_{ND}$ . These uncertainties mostly arise from the differences in event selection between the two detectors and in particular the modelling of the energy scales. These are also virtually nonexistent in the case that ND and FD are identical.
- *Differences in the neutrino flux*  $\Phi_{FD}/\Phi_{ND}$ . The fluxes at the Near and Far detector are radically different since the ND is very close to the beamline and sees an expended source, while the FD is 1300 km away. A Monte Carlo is used to simulate the beam propagation, but it is itself not immune from inaccuracies: errors in the hadron production, focusing of the horns composition of the beam pipe and decay channel geometry can all contribute.

Source of Uncertainty	MINOS Absolute/ $\nu_e$	T2K $\nu_e$	LBNE $\nu_e$	Comments
Beam Flux after N/F extrapolation	3%/0.3%	2.9%	2%	MINOS is normalization only. LBNE normalization and shape highly correlated between $\nu_\mu/\nu_e$ .
Detector effects				
Energy scale ( $\nu_\mu$ )	7%/3.5%	included above	(2%)	Included in LBNE $\nu_\mu$ sample uncertainty only in three-flavor fit. MINOS dominated by hadronic scale.
Absolute energy scale ( $\nu_e$ )	5.7%/2.7%	3.4% includes all FD effects	2%	Totally active LArTPC with calibration and test beam data lowers uncertainty.
Fiducial volume	2.4%/2.4%	1%	1%	Larger detectors = smaller uncertainty.
Neutrino interaction modeling				
Simulation includes: hadronization cross sections nuclear models	2.7%/2.7%	7.5%	$\sim 2\%$	Hadronization models are better constrained in the LBNE LArTPC. N/F cancellation larger in MINOS/LBNE. X-section uncertainties larger at T2K energies. Spectral analysis in LBNE provides extra constraint.
Total	5.7%	8.8%	3.6 %	Uncorrelated $\nu_e$ uncertainty in full LBNE three-flavor fit = 1-2%.

Table 2.1: Dominant systematics on the  $\nu_e$  appearance channel for T2K and MINOS and projection for LBNE (Long Baseline Neutrino Experiment), the preliminary name used for DUNE [46]

Taking all of this into consideration one can then use neutrinos' oscillation and survival probability in order to predict the muonic and electronic signal in the Far Detector. The  $\nu_\mu$  expected signal is given by:

$$N_{FD}^{exp}(\nu_\mu) = N_{ND}^{data}(\nu_\mu) \otimes \frac{\Phi_{FD}(\nu_\mu)}{\Phi_{ND}(\nu_\mu)} \otimes P(\nu_\mu \rightarrow \nu_\mu) \otimes \frac{\varepsilon_{FD}(\nu_\mu)}{\varepsilon_{ND}(\nu_\mu)} \otimes \frac{\sigma_{FD}(\nu_\mu)}{\sigma_{ND}(\nu_\mu)} \quad (2.2)$$

The  $\nu_e$  expected signal is given by:

$$\begin{aligned} N_{FD}^{exp}(\nu_\mu) &= N_{ND}^{data}(\nu_\mu) \otimes \underbrace{\frac{\Phi_{FD}(\nu_\mu)}{\Phi_{ND}(\nu_\mu)} \otimes P(\nu_\mu \rightarrow \nu_e) \otimes \frac{\varepsilon_{FD}(\nu_e)}{\varepsilon_{ND}(\nu_\mu)} \otimes \frac{\sigma_{FD}(\nu_e)}{\sigma_{ND}(\nu_\mu)}}_{\text{Expected signal}} \\ &+ N_{ND}^{data}(\nu_e) \otimes \underbrace{\frac{\Phi_{FD}(\nu_e)}{\Phi_{ND}(\nu_e)} \otimes P(\nu_e \rightarrow \nu_e) \otimes \frac{\varepsilon_{FD}(\nu_e)}{\varepsilon_{ND}(\nu_e)} \otimes \frac{\sigma_{FD}(\nu_e)}{\sigma_{ND}(\nu_e)}}_{\text{Electronic events from the beam}} \\ &+ \pi^0 \text{NC background prediction from } N_{ND}^{data}(\nu_e) \\ &+ \nu_\tau \text{ background prediction from } N_{ND}^{data}(\nu_\mu) \end{aligned} \quad (2.3)$$

The main sources of uncertainties are well known from previous experiments such as T2K and MINOS. They include:

- *Beam flux uncertainties*: related to the precision with which the ND is capable to measure the unoscillated beam flux in both shape and normalization.
- *$\nu_\mu$  energy-scale uncertainties*: the muonic neutrino energy spectrum measured in the ND is then used to predict the  $\nu_e$  appearance channel in the FD and the energy scale uncertainty scale is thus propagated.
- *Absolute  $\nu_e$  energy-scale uncertainty*: an accurate measurement of the shape of the  $\nu_e$  appearance channel is essential to oscillation sensitivity and depends on how well the detector response is understood
- *Simulation uncertainties*: uncertainties related to the modelling of the neutrino interactions with the target nuclei in the near and far detectors.

In Table 2.1 the dominant uncertainties for  $\nu_e$  appearance for the T2K and MINOS and a preliminary prediction for DUNE are summarized. The precision is expected to improve from all fronts.

### 2.1.2 Mass ordering and $\delta_{CP}$

As it can be seen from Eq. 1.25 both a non-zero  $\delta_{CP}$  and matter effects can induce asymmetries between  $P(\nu_\mu \rightarrow \nu_e)$  and  $P(\bar{\nu}_\mu \rightarrow \bar{\nu}_e)$  and thus:

$$\mathcal{A}_{CP} = \mathcal{A}_\delta + \mathcal{A}_{matter} \quad (2.4)$$

In figure 2.2 the asymmetries induced by CP violation ( $\mathcal{A}_\delta$ ) in case that  $\delta_{CP} = \pm\pi/2$  and by matter effects ( $\mathcal{A}_{matter}$ ) are plotted separately in 2d oscillograms as a function of baseline and Energy. In reality though the two asymmetries always operate at the same time if  $\delta_{CP}$  is not null and the matter effects are not trivial. In experiments where both are relevant then, if one wants to use measurements of total asymmetry both to measure  $\delta_{CP}$  and the mass ordering, then it's mandatory to be able to disambiguate between the two [47].

For the MSW effects in particular the asymmetries are introduced by a CP violating term  $P_{\sin \delta}$  in the oscillation probability:

$$P(\nu_\mu \rightarrow \nu_e) \simeq P(\nu_e \rightarrow \nu_\mu) \simeq P_0 + P_{\sin \delta} + P_{\cos \delta} + P_3 \quad (2.5)$$

where

$$P_0 = \sin^2 \theta_{23} \frac{\sin^2 2\theta_{13}}{(A - 1)^2} \sin^2[(A - 1)\Delta] \quad (2.6)$$

$$P_3 = \alpha^2 \cos^2 \theta_{13} \frac{\sin^2 2\theta_{12}}{A^2} \sin^2(A\Delta) \quad (2.7)$$

$$P_{\sin \delta} = \alpha \frac{8J_{CP}}{A(1-A)} \sin \Delta \sin(\Delta A) \sin((1-A)\Delta) \quad (2.8)$$

$$P_{\cos \delta} = \alpha \frac{8J_{CP} \cot \delta_{CP}}{A(1-A)} \sin \Delta \sin(\Delta A) \sin((1-A)\Delta) \quad (2.9)$$

with

$$\Delta = \Delta m_{31}^2 L / 4E \quad (2.10)$$

$$A = \sqrt{3} G_F N_e 2E / \Delta m_{31}^2 \quad (2.11)$$

$$\alpha = |\Delta m_{12}^2| / |\Delta m_{31}^2| \quad (2.12)$$

Note that since the value of  $\Delta m_{31}^2$  switches between normal and inverted hierarchy, the asymmetry effects induced by the passage through matter will also be different: for normal (inverted) hierarchy  $P(\nu_\mu - \nu_e)$  is enhanced (suppressed) and  $P(\bar{\nu}_\mu - \bar{\nu}_e)$  is suppressed (enhanced); the matter effects shift the phase of oscillation pattern for a fixed baseline to lower energies (by about -100 MeV) in the IH.

In general the matter effects have the largest impacts when the oscillation nodes for  $\theta_{13}$  are reached (the first two nodes are highlighted in black in Fig. 2.2):

$$\frac{L(\text{km})}{E(\text{GeV})} = (2n-1) \frac{\pi}{2} \frac{1}{(1.27 \times \Delta m_{31}^2 (\text{eV}^2))} \simeq (2n-1) \times 510 \text{km/GeV} \quad (2.13)$$

For an experiment such as DUNE, where we have a baseline of  $L \sim 1300 \text{ km}$  (highlighted in black in Fig. 2.2) and an energy range  $E \sim 5 - 10 \text{ GeV}$ , the matter effects are maximal, and it is then crucial that they are disentangled from the CP effects.

Knowing the value of  $|\Delta m_{31}^2|$  (only the sign is still unknown), one can see, though, that for a baseline  $> 1200 \text{ km}$ , the size of  $\mathcal{A}_{\text{matter}}$  surpasses the highest possible value of  $\mathcal{A}_\delta$  which makes the disambiguation between the two effects possible. In Figure the plots show the total asymmetry at the first (black) and second (red) as a function of  $\delta_{CP}$  for four different values of  $L$ : 290km, 810km, 1300km (baseline of DUNE) and 2300km. The NH and IH the total asymmetries will have different values because of the matter effects and are plotted as full and dashed lines respectively. As the baseline gets bigger, given the same node, the CP-induced asymmetry will stay the same while matter induced one will get bigger since the dependencies on  $L$  and  $E$  are:

$$\mathcal{A}_\delta \propto L/E \quad (2.14)$$

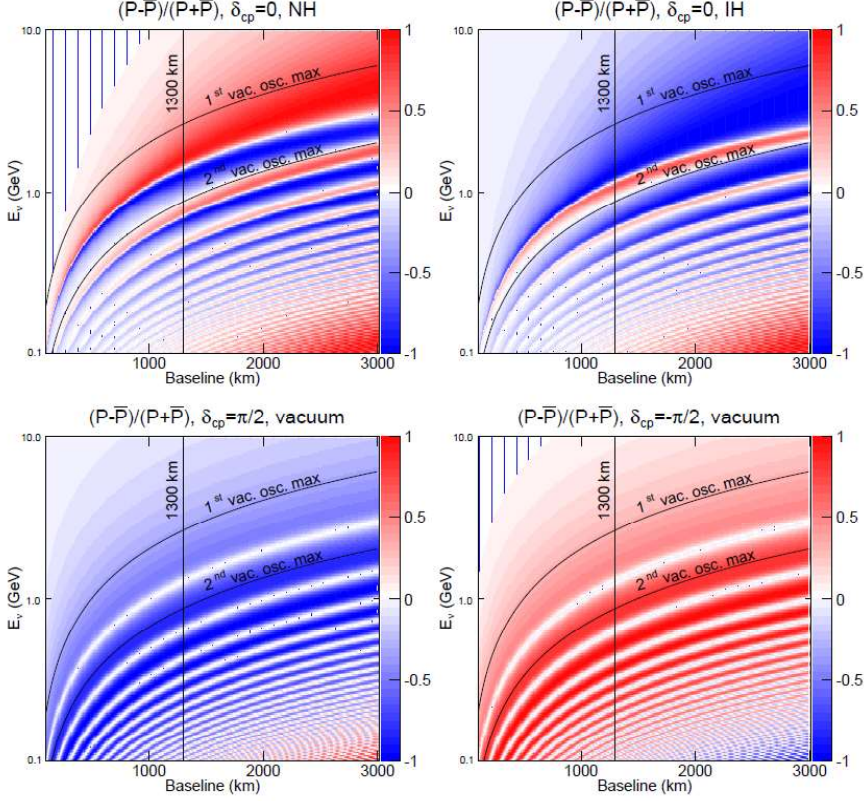


Figure 2.2:  $\mathcal{A}_{CP}$  total asymmetry as a function of baseline and energy. The top two oscillograms show the asymmetry for  $\delta_{CP} = 0$  (i.e.  $\mathcal{A}_{matter}$ ) for Normal(left) and Inverted (right) mass ordering. The two bottom oscillograms show the asymmetry in vacuum (i.e.  $\mathcal{A}_\delta$ ) for  $\delta_{CP} = \pi/2$  (left) and  $\delta_{CP} = -\pi/2$  (right). DUNE’s baseline (1300km) and the 1st and 2nd oscillation nodes are highlighted in black. [47]

$$\mathcal{A}_{matter} \propto L \times E \quad (2.15)$$

If one considers then the case in which the  $\delta_{CP}$  asymmetries is maximal (green line in the plots) is easy to see that if  $\mathcal{A}_{matter} < \mathcal{A}_\delta(\max)$  the same total asymmetry is compatible with both hierarchies and multiple value of  $\delta_{CP}$ . This is true for baselines shorter than 1200km. For DUNE, where  $L \sim 1300\text{km}$  these ambiguities don’t exist.

### Significance for mass ordering and $\delta_{CP}$ measurements

The sensitivity with which the DUNE experiment will be able to measure the mass ordering (MO) and CP-Violation (CPV), is evaluated by fitting the

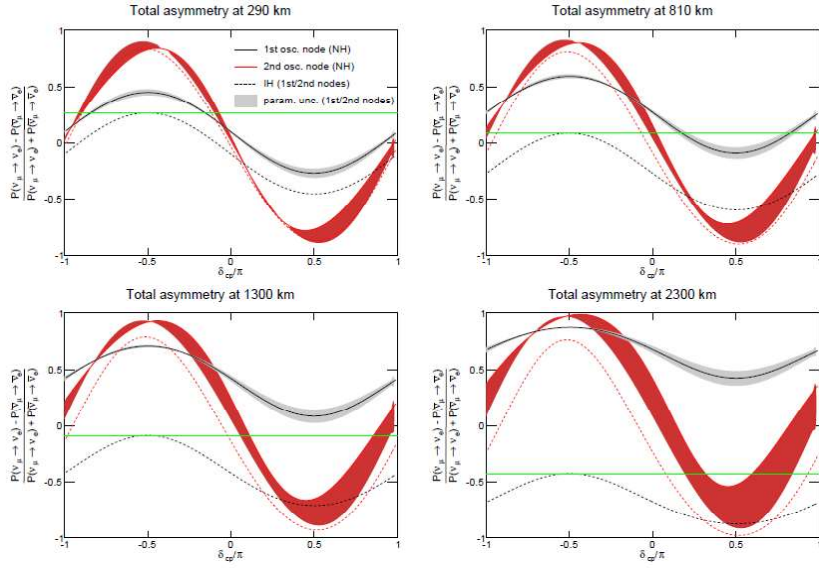


Figure 2.3: Total  $\mathcal{A}_{CP}$  as a function of  $\delta_{CP}/\pi$  for four different baselines (290km, 810km, 1300km and 2300km). The black (red) lines indicate the asymmetries at the first (second) node, the full ones being for NH and the dashed ones for IH. [47]

simulated oscillation spectra of  $\nu_\mu \rightarrow \nu_{\mu,e}$  and  $\bar{\nu}_\mu \rightarrow \bar{\nu}_{\mu,e}$  for different values of the oscillation parameters and confronting the results with the expected "true" theoretical values in terms of  $\Delta\chi^2$ :

$$\Delta\chi^2_{MO} = |\chi^2_{MH^{test}=IH} - \chi^2_{MH^{test}=NH}| \quad (2.16)$$

$$\Delta\chi^2_{CPV} = \min(\Delta\chi^2_{CP}(\delta_{CP}^{test} = 0), \Delta\chi^2_{CP}(\delta_{CP}^{test} = \pi)) \quad (2.17)$$

with  $\Delta\chi^2_{CP} = \chi^2(\delta_{CP}^{test}) - \chi^2(\delta_{CP}^{true})$ . The significance with which DUNE will be able to assess the mass ordering grows with the exposure , defined as  $kt$  of active volume  $\times$  MW beam? s power  $\times$  years, and varies wildly with the value of  $\delta_{CP}$  (Fig.2.4). In order to ensure the DUNE objective of reaching  $\sqrt{\Delta\chi^2} = 5$  for every value of  $\delta_{CP}$  approximately an exposure of 200-400  $kt \times MW \times years$  will be need. The significance for  $\delta_{CP}$  similarly grows with exposure (Fig.2.6), but only for values different from 0 and  $\pi$ , for which there is no CP violation and  $\sqrt{\Delta\chi^2} = 0$  always. The significance for both MO and CPV also depends strongly on the values of all the oscillation parameters (Fig. 2.5 and 2.7), making precision measurements with DUNE mandatory.

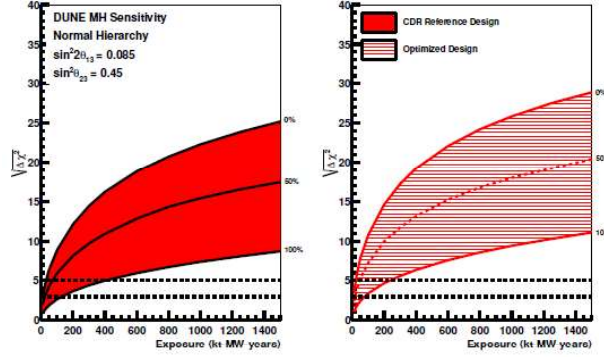


Figure 2.4: MO significance as a function of exposure for two different beam designs (left and right) and three values of CP asymmetry (0%, 50%, 100%). [47]

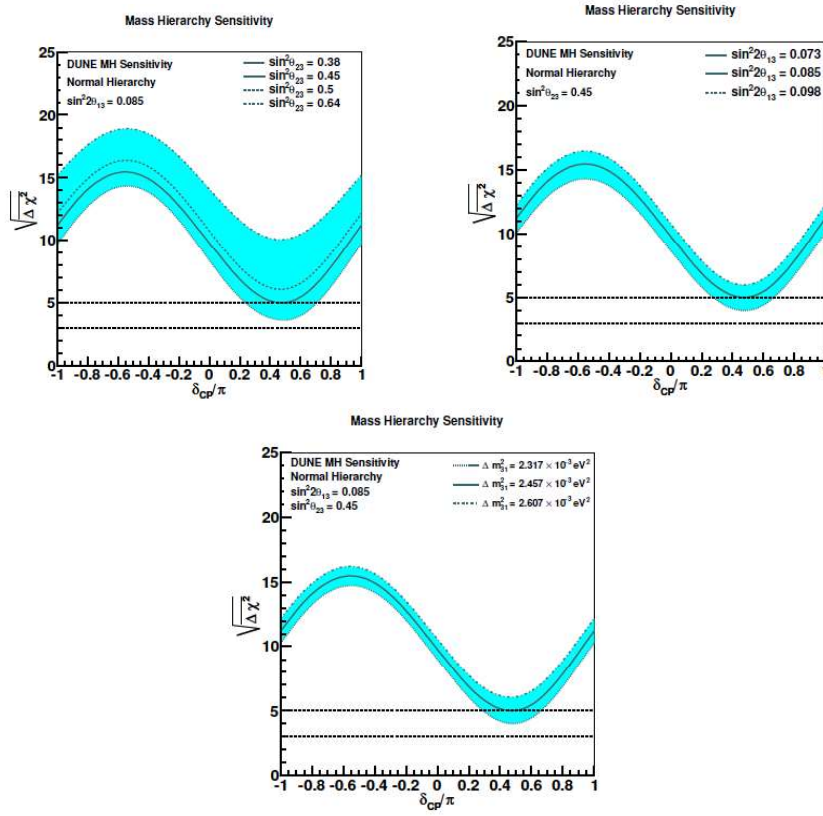


Figure 2.5: MO significance as a function of  $\delta_{CP}/\pi$  at a fix value of exposure 300 kt  $\times$  MW  $\times$  years for different values of the oscillation parameters:  $\theta_{23}$  (upper-left),  $\theta_{13}$  (upper-right),  $\delta m_{31}^2$  (bottom) [47]

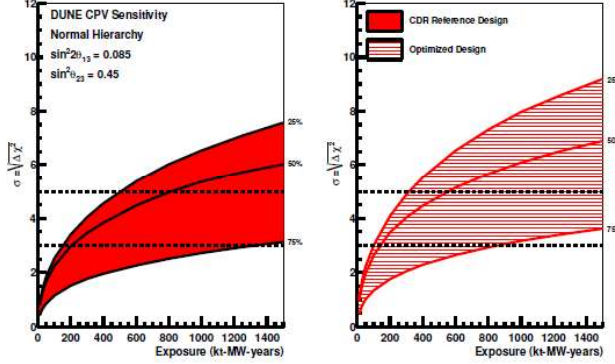


Figure 2.6: CPV significance as a function of exposure for two different beam designs (left and right) and three values of CP asymmetry (0%, 50%, 100%). [47]

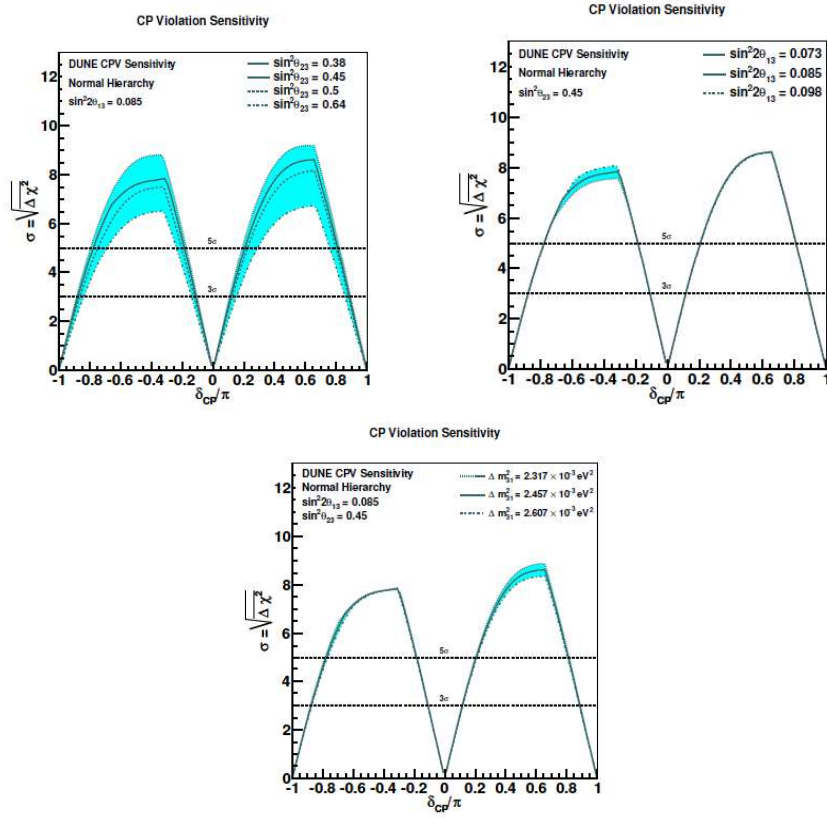


Figure 2.7: CPV significance as a function of  $\delta_{CP}/\pi$  at a fix value of exposure 300  $kt \times MW \times years$  for different values of the oscillation parameters:  $\theta_{23}$  (upper-left),  $\theta_{13}$  (upper-right),  $\Delta m_{31}^2$  (bottom) [47]

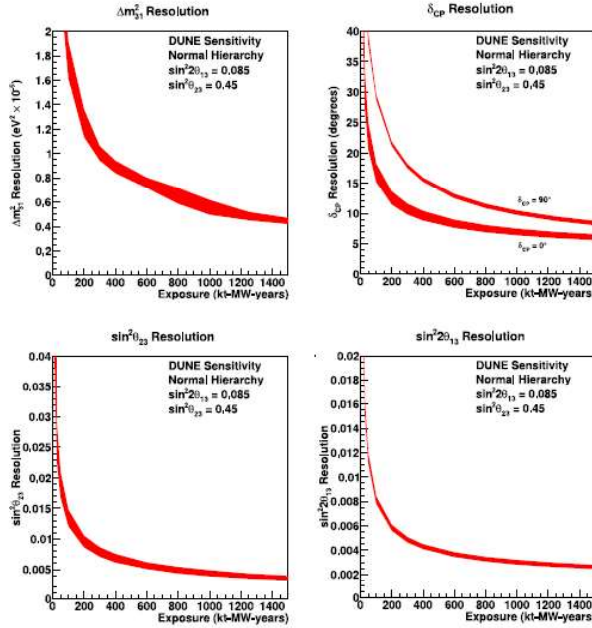


Figure 2.8: Resolution as a function of exposure for  $\Delta m_{31}^2$  (upper left),  $\delta_{CP}$  (upper right),  $\sin^2 \theta_{23}$  (bottom left) and  $\sin^2 \theta_{13}$  (bottom right). The red area represents the range in sensitivity due to differences in beam design. [47]

### 2.1.3 Precision measurements

The DUNE experiment will improve sensitivity on the key parameters governing  $\nu_1 - \nu_2$  and  $\nu_2 - \nu_3$ :

- $\sin^2 \theta_{23}$  and the octant of  $\theta_{23}$ ;
- $\delta_P$ ;
- $\sin^2 \theta_{13}$ ;
- $\Delta m_{31}^2$ .

The sensitivity to these parameters as a function of exposure is plotted in Figure 2.8

Determining the octant of the mixing angle  $\theta_{23}$ , and thus if its value is exactly  $45^\circ$  producing maximal mixing between mass eigenstates 2 and 3  $\sin^2 \theta_{23}$  is still an open question, with the latest results from T2K leaving both a lower ( $< 45^\circ$ ) and upper ( $< 45^\circ$ ) octant scenarios open, depending on the mass hierarchy being considered. This particular question is of great theoretical interest. A value of  $\theta_{23}$  being exactly  $45^\circ$  would hint at new nt yet considered

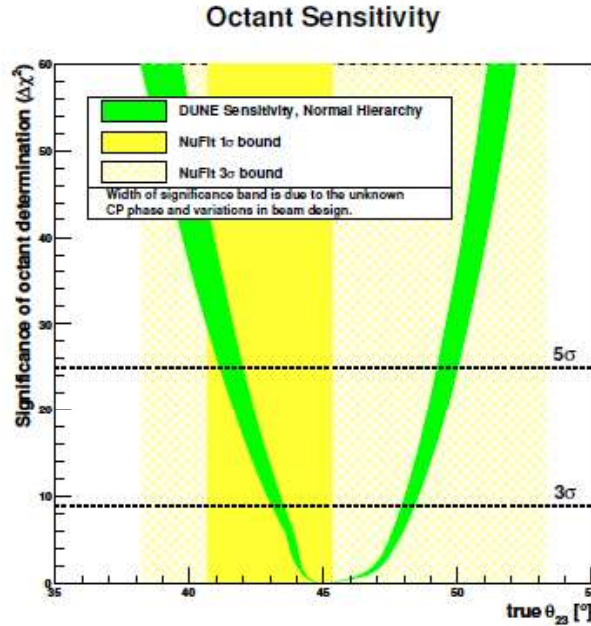


Figure 2.9:  $\Delta\chi^2_{octant}$  as a function of  $\theta_{23}$ . The yellow areas indicate the  $1\sigma$  and  $3\sigma$  intervals for the value of  $\theta_{23}$  from recent global fits. The green area represents the range in sensitivity due to differences in beam design and  $\delta_{CP}$  value.[46]

symmetries, while for example an excess in the upper octant of the order of the Cabibbo angle, point in the direction of quark-lepton universality models. The measurement of the octant is made possible by combining survival ( $\nu_\mu \rightarrow \nu_\mu$ ) and oscillation ( $\nu_\mu \rightarrow \nu_e$ ) probabilities, the first being sensitive to  $\sin^2 2\theta_{23}$  and the second to  $\sin^2 \theta_{23}$ . The  $\Delta\chi^2$  for the determination of the octant is then:

$$\Delta\chi^2_{octant} = |\chi^2_{\theta_{23}>45^\circ} - \chi^2_{\theta_{23}<45^\circ}| \quad (2.18)$$

The sensitivity to the octant as a function of  $\theta_{23}$  is plotted in Fig.2.9. DUNE will also be able to perform unitarity tests of the PMNS matrix by measuring precisely the value of  $\sin 2\theta_{13}$ , which will constrain the phase space of possible new physics. In general the high precision measurement performed by dune could reveal new physics driven for example by non-standard interactions or the existence of sterile neutrinos.

### 2.1.4 Proton decay measurements

Almost all Grand Unified Theories (GUTs) predict some sort of proton decay and baryon number non conservation. Detecting a proton decay would

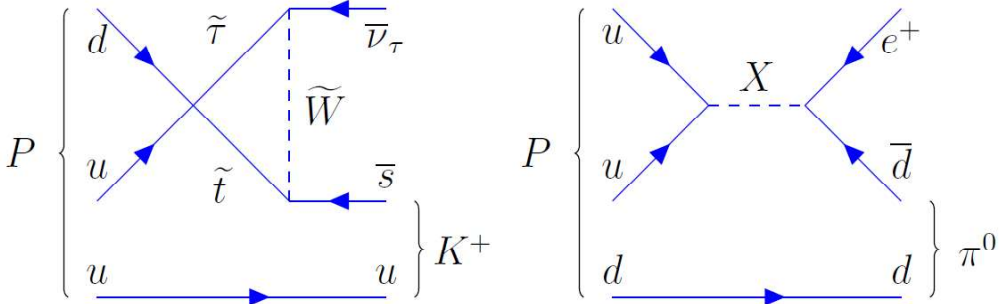


Figure 2.10: Feynman diagrams for two major proton decay modes: the main decay for SUSY GUTs  $p^+ \rightarrow K^+ \bar{\nu}$  (left) and the main decay for gauge-mediation GUTs  $p^+ \rightarrow e^+ \pi^0$  (right)[46]

be in fact one of the only viable experimental strategies to probe these theories since the unification scale is in excess of about  $10^{15}$  GeV with respects to energies accessible to accelerator experiments. Early GUT theories were in fact one of the main motivations behind the construction of underground kt-scale experiments such as Kamiokande, as already mentioned in Section 1.4. The non-detection of proton decay set proton life-time constraints and progressively rule out theories based on their predictions. The most recent limits set by Super-Kamiokande have in fact confirmed the ruling out of minimal SU(5) (previously established by IMB and Kamiokande) and has disproved minimal SUSY SU(5). The next generation of large underground experiment such as Hyper-Kamiokande and DUNE will be well equipped to continue the search and, at the very least, make the constraints more stringent.

From the theoretical body of work, two main decay mode emerge, the first from supersymmetric GUTs and the second from gauge-mediated GUTs (see Fig. 2.10 for the Feynmann diagrams):

$$p^+ \rightarrow K^+ \bar{\nu} \quad (2.19)$$

$$p^+ \rightarrow e^+ \pi^0 \quad (2.20)$$

The first decay mode is especially interesting for large LArTPCs (such as the FD of DUNE) since it presents a kaon in its final state: kaons have an especially high ionization rate and would be detected with great efficiency using liquid Argon technologies. The second one is perhaps better known and has its most clear signature in Cherenkov detectors, since it consists of an electromagnetic shower ignited by the the  $e^+$  and two  $\gamma$  from the  $\pi^0$  decay.

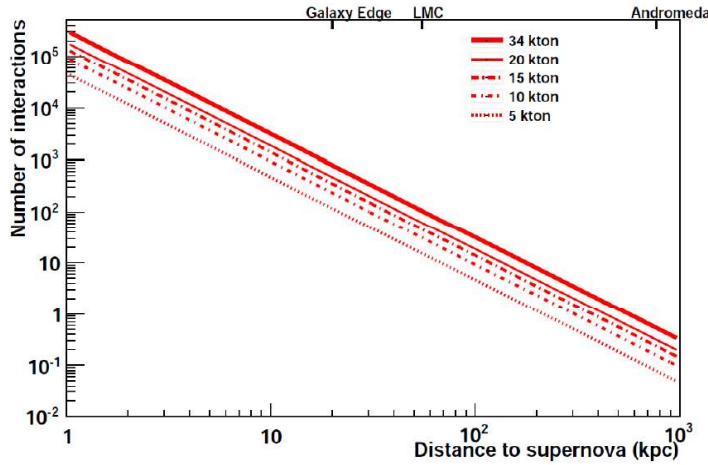


Figure 2.11: Number neutrino interactions from supernova explosions, as a function of distance, for different volume LArTPCs.[46]

### 2.1.5 Supernova neutrino measurements

Given an experimental life of 20 years, DUNE would have about a 40% chance of observing neutrinos from a core collapse Supernova in the Milky Way. This would be of great importance for our understanding of this astrophysical phenomenon, which as of now only been confirmed in its basic characteristics by the observation of neutrino events from SN1987, a supernova in the Large Magellanic Cloud, 50 kpc away.

Supernovas also promise an extremely varied environment to study neutrino oscillation, with their initial flavour composition being strictly linked to the expanding shock and turbulence. For example the oscillation patterns would be very different for NH and IH ;the oscillations of neutrinos and anti-neutrinos would also manifest rather differently, making the observation of both with high statistics of particular interest.

While water Cherenkov detectors are more sensitive to  $\bar{\nu}_e$ , LArTPCs are primarily sensitive to  $\nu_e$ , making them complementary in Supernova detection. The unique sensitivity to electron neutrinos of Argon detectors is due to the absorption channel on Argon:



This interaction can be in principle detected exploiting the coincidence of the gamma cascade produced by the de-excitation of  ${}^{40}\text{K}^*$  and the electron. The plot in Figure 2.11 shows the number neutrino interactions from supernova explosions, as a function of distance, for LArTPCs of different volumes. For

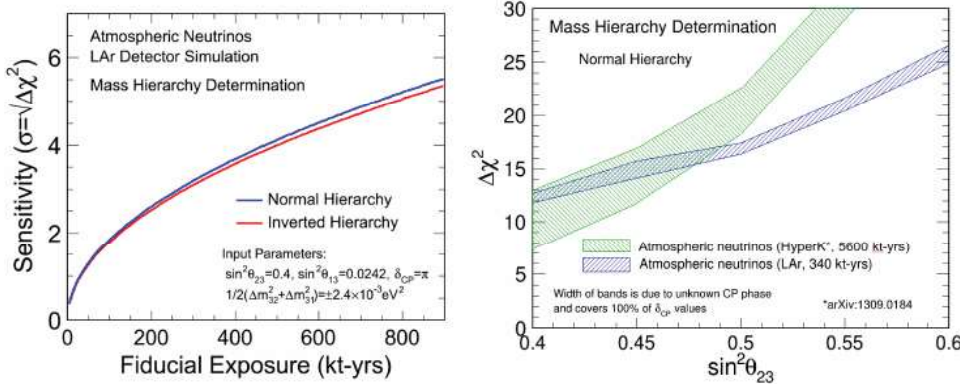


Figure 2.12: (*Left*) MO sensitivity for the atmospheric neutrino sample as a function of exposure for both NH (blue) and IH (red); (*Right*) MO sensitivity for the atmospheric neutrino sample as a function of the true value of  $\theta_{23}$  in NH, with values for Hyper-K given for comparison.[48]

a detector of 10 kt, about the size of the FD of DUNE, a Supernova explosion at the likely distance of about 10 kpc would produce about 900 events. Only 19 events from two Cherenkov detectors and a few more from scintillation detectors were registered for SN1987A.

### 2.1.6 Oscillation physics with atmospheric neutrinos

DUNE’s Far Detector, given its 10kt volume and being  $\sim 1500$  m underground (sufficient for cosmic ray shielding), will be well equipped to do oscillation measurements using atmospheric neutrinos. Given that the atmospheric sample contains  $\nu$ ’s of all flavours over a vast range of energy and path length including some for which matter effects are relevant, all oscillation parameters could be measured, offering a very useful complementary program to the main accelerator one.

Measuring atmospheric oscillations would also be very useful in the field of mass ordering determination. The MO sensitivity , using the atmospheric neutrino sample, goes as the square root of the exposure and is thus not limited by systematics. Additionally it is dependent on the value of  $\sin^2 \theta_{23}$  offering an alternative method of measuring  $\theta_{23}$  and its octant.

Finally, new physics searches are also possible in the atmospheric sector, with previous experiments having set limits on CPT violation, non-standard interactions, Lorentz-invariance violation and neutrino mass variance.

### 2.1.7 Near detector physics

The Near detector main goal will be to provide precision measurements necessary to take into account the systematic uncertainties typical of a long baseline neutrino experiments. These measurements include the characterization of the neutrino flux and its energetic spectrum and flavour composition, which is mandatory to make predictions on the far/near flux ratio. It will also measure the secondary hadrons produced in NC and CC interactions, which are the dominant component of the oscillation background.

Since the near detector will be subjected to a high statistic of neutrino interactions it will also have an independent program, focused on flux measurements of fluxes, cross sections and particle production over a wide energetic range (0.5-50 GeV). Of particular importance will be the evaluation of the neutrino-Argon cross section and the characterizations of the various interaction channels.

Finally the large samples of events to which the Near Detector will be subjected can be exploited for sensitive studies in the electroweak sector and the search for new physics. Some of these endeavours can include for example the search for heavy sterile neutrinos with large oscillation  $\Delta m^2$  of the order of 1 eV<sup>2</sup>, for which some indications already exist. The ND will also be able to look for light dark matter WIMP-like particles. These could be distinguished from neutrino signatures by using timing information, assuming that the WIMPS are much heavier than the neutrinos and travel slower through matter, and spacial informations.

## 2.2 LBNF/DUNE's facilities and design

The experimental facilities and detectors will be divided between the Long-Baseline Neutrino Facility (LBNF), hosted by Fermilab and the DUNE collaboration. The first will provide the facilities in Illinois (Near Detector Facilities) and South Dakota at SURF (Far Detector facilities), necessary for the scientific program of DUNE. The collaboration will supervise the NuMI neutrino beam with the necessary upgrades, the ND conventional facilities in Fermilab and the construction of the caverns necessary to host the four liquid Argon far detectors. The DUNE collaboration will overview the design and construction of the detectors themselves. [50]

### 2.2.1 FD reference design: single phase LArTPC

The reference design for DUNE's Far Detector consists of four 10 kt single-phase Liquid Argon Time projection chambers (for a total fiducial mass of

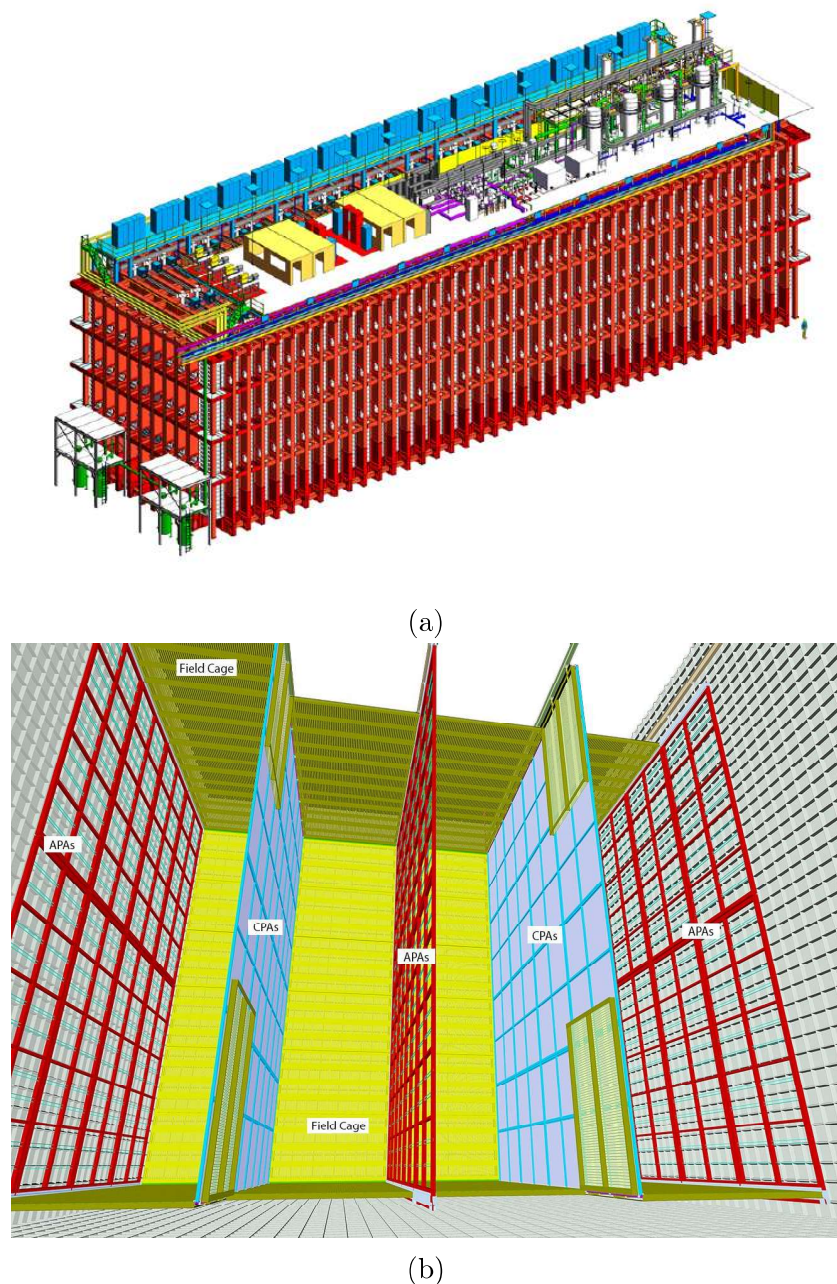


Figure 2.13: 3D Model of the FD single-phase reference design seen from outside (a) and inside of the TPC (b) [50]

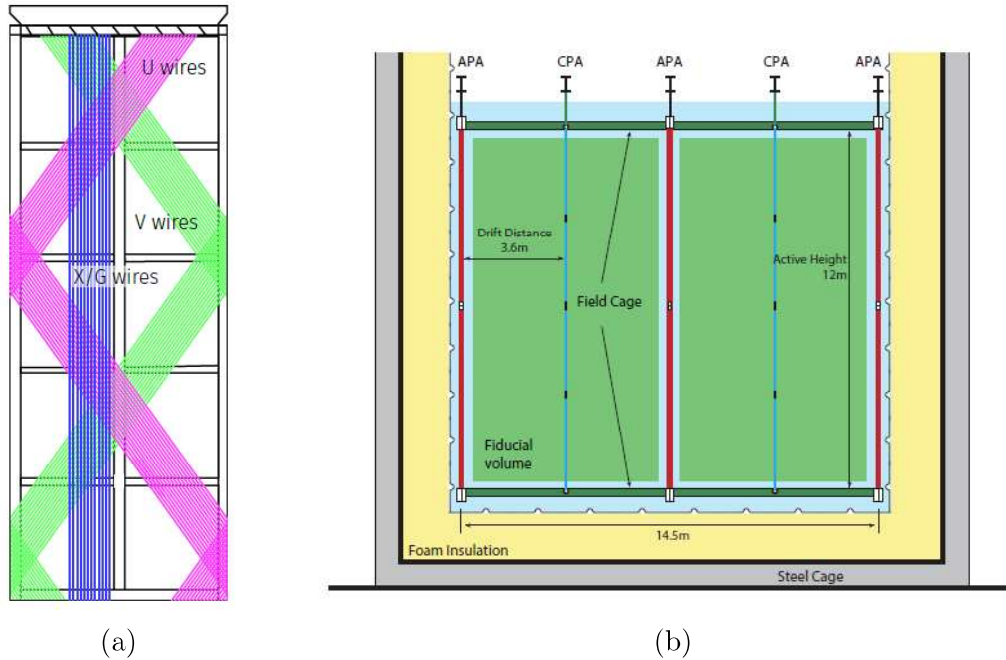


Figure 2.14: (a) Wiring scheme of an APA module (b) Front schematic view of the inside of the TPC [50]

40kt), each suspended inside a cryostat and augmented with a photon detection system (A model of the reference design is shown in Fig 2.13).

The LArTPC technology will be extrapolated from the pioneering techniques used by ICARUS. The charged particles in liquid Argon (LAr) produce ionization and scintillation light. The electrons drifting from the cathode plane towards the segmented anode plane produce a signal then used to provide spatial information. The prompt scintillation photons are collected by a photon detection system that provide the absolute timing of the event. In particular a detector is single-phase if the ionization, drift and collection all occur in Liquid Argon.

The two main active components of the detector are then the actual Time Projection Chamber (TPC) and the Photon Detection System (Photon Detector System), with the electronics divided in Cold Electronics (CE), mounted inside the Liquid Argon TPC, and the rest of the Data Aquisition System (DAQ).

### The time projection chamber (TPC)

The TPC is the fundamental detector of DUNE's FD design. It is located inside an external cryostat keeping its temperature at 88 K (necessary

Label	Function	Orientation (from vertical)	Pitch (mm)	Number	Bias Voltage (volt)
G	Shield/grid plane	0°	4.79	960	-655
U	1 <sup>st</sup> induction plane	+35.7°	4.67	800	-365
V	2 <sup>nd</sup> induction plane	-35.7°	4.67	800	0
X	Collection plane	0°	4.79	960	+860

Table 2.15: Bias voltage, orientation and pitch of the APA wire layers [50]

to keep the Argon in its liquid phase) and is built modularly from by anode plane assemblies (APA), cathode plane assemblies (CPA) and field cage modules. The APAs and CPAs are assemblies of wire planes and are placed in rows, parallel to the beam direction, to form three anode planes and two cathode planes respectively. Each anode plane is made of 25 vertical stacks of two 6m heigh and 2.3m wide APAs, while the cathode planes are equal in total size but double the number of CPAs, which are half the height of the anodic assemblies. The field cage modules close the four open sides left between the alternating vertical planes with the total structure being 12m heigh, 14.5m wide and 58 m long. A "slice" of the TPC, perpendicular to the beam direction, is shown in Figure 2.14 (b).

The APAs are built on each side of a lightweight rectangular frame and include four wire layers: from outside a shielding plane (G), two induction planes (U and V) and the collection plane (X). The CE front-end electronics are mounted directly on the module's frame. The wiring scheme is shown in Figure 2.14 (a).

The APAs and CPAs are set to a specific voltage so that an electric field, kept uniform by the field cage, is formed perpendicularly between the planes. When a charged particle traverses the chamber, it then forms a trail of ionized electrons and ions: these will then start drifting in opposite directions following the field lines. The electrons will drift towards the closest anode planes inducing an electric current signal in the electronics. The maximum electron-drift distance is set to 3.6m by applying a bias voltage to the cathodes of -180kV in order to obtain a nominal drift field of 500 V/cm. Note that each APA's wire layer is set to a specific voltage so that the ionization electrons drift past the first three and are collected exclusively in X (Table 2.15).

The waveforms are then digitized and sent through cold-resisting cables to the DAQ outside the cryostat. The DAQ system is designed to have high uptime of data collection (> 99%) for all types of interactions the detector is

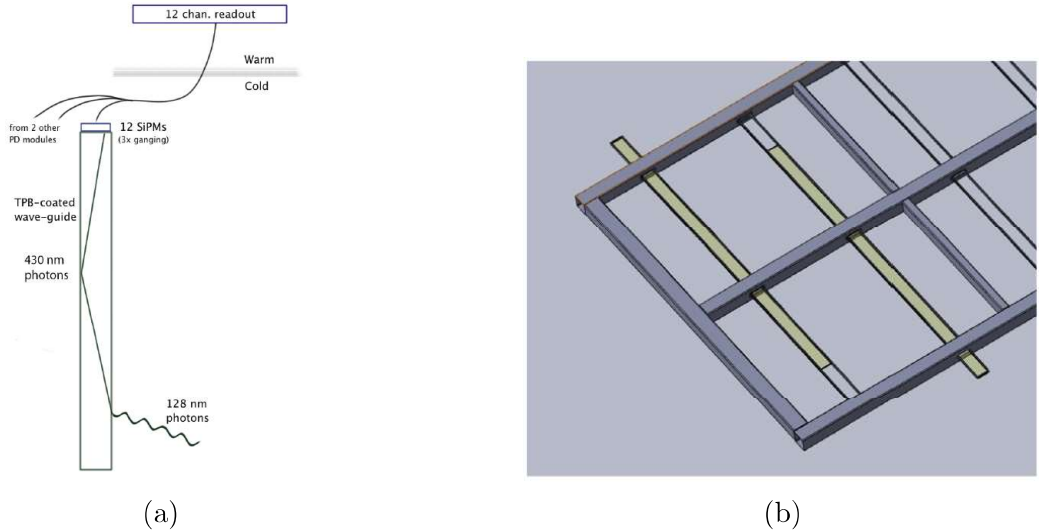


Figure 2.16: (a) Schematic representation of a PD module from the reference design (b) Positioning of the reference PD modules in the APA frame [50]

trying to detect: beam and atmospheric neutrino and proton decay products. The DAQ of each 10kt module is for this reason left independent reducing dead-time significantly.

### Photon detection system

A charged particle depositing 1 MeV in LAr will generate on average 40000 photons of wavelength roughly 128 nm,(VUV) to which the liquid Argon medium is highly transparent. About a fourth of them will be prompt photons emitted almost immediately (average lifetime  $\sim 6$  ns), with the rest being emitted after 1100-1600 ns. The high light-yield makes the scintillation process ideal for determining the  $t_0$  of non-beam related events, such as proton decay candidates and supernova or atmospheric neutrinos.

The reference Photon Detection system consists of modules to be mounted on the APA frames (Figure 2.16). They would consist of a light-guide and 12 Silicon Photo-multipliers (SiPM). The light-guide bar is painted with a wavelength shifter peaked at 430 nm, in order to match the maximum efficiency of the SiPMs. Each APA would host ten PD modules, positioned at equispaced intervals along the length of the anode module, each being 2.2 m in length, 83 mm wide and 6 mm thick.

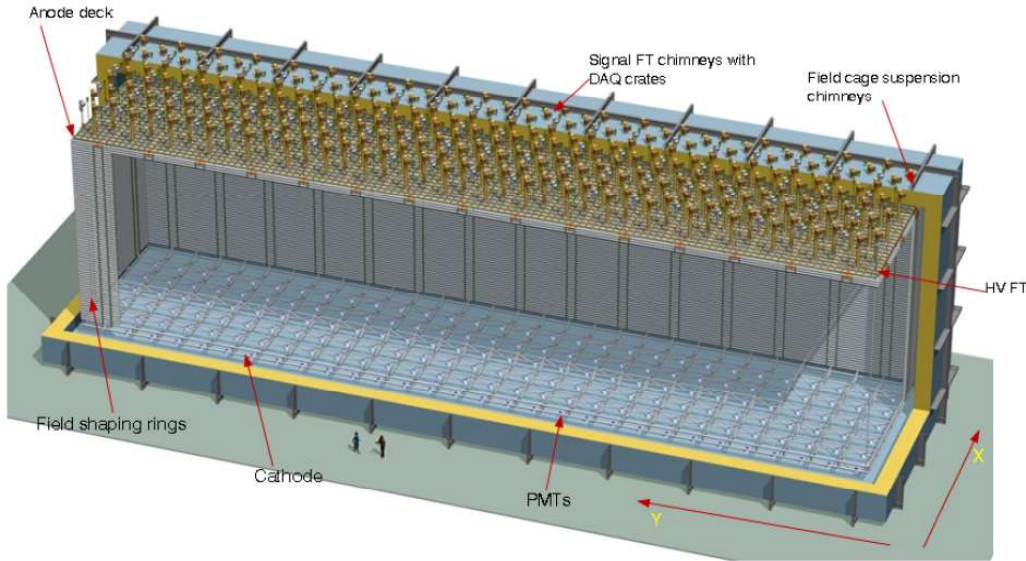


Figure 2.17: 3D model of the dual-phase LArTPC alternative design [50]

### 2.2.2 FD alternative design: double phase LArTPC

In addition to the reference design, which has already been chosen as the model for the first FD module, an alternative dual phase design, augmented with a light collection system, is being considered for the other three. In a dual phase LArTPC, the ionization electrons are produced in a tank filled with fully homogenous liquid argon, then drifted upwards towards an extraction grid just below a gaseous argon volume. They are then extracted, amplified via Townsend multiplication and finally collected on a finely segmented anode. This sort of design has several advantages, such as a generally higher gain and consequently a better signal to noise ratio (S/N), a larger fiducial volume and longer drift path and a lower detection threshold.

A 100 % extraction efficiency is achieved applying a 2kV/cm electric field between the extraction grid ( made of stainless steel wires, 1mm in diameter and spaced by 3.125mm ) and the amplification devices placed in ultra pure Argon gas. These devices, called Large Electron Multipliers (LEMs) are 1mm circuit boards placed between two electrodes, micro-patterned with tiny holes. Between the electrodes electron avalanches are induced by applying a 3kV potential difference. It is this feature in particular that improves the S/N ratio by at least an order of magnitude and lowers the threshold for energy deposition, improving resolution. The 2D finely segmented collection anode is placed on top of the gas phase volume and is connected to the first level of electronics.

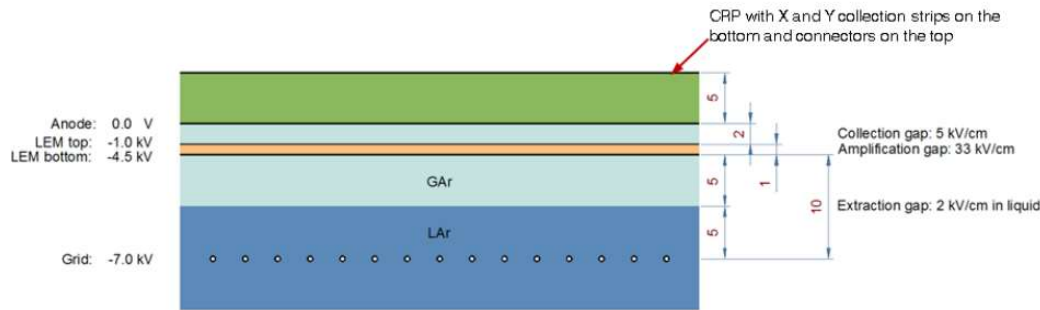


Figure 2.18: Schematic representation of a CRP module with thickness and voltage values for a 0.5 kV/cm drift field in liquid Argon. [50]

The collection grid, LEM and anode elements are segmented in  $0.5 \times 0.5\text{m}^2$  sections and combined to form independent modules called Charge readout PLANES (CRPs), which are embedded in a FR-4 and stainless steel armour. These are suspended from the roof of the tank and cover the entire upper surface. Combined with PMT arrays, collecting the scintillation light for timing information, a CRP module provides 3D position and calorimetric reconstruction. A schematic representation of these elements is shown in Figure 2.18.

The cathode layer, to which the high voltage that produces the drift field ( $E_{drift} \sim 0.5 \text{ kV/cm}$ ) covers the tank's floor. The field is kept homogenous by a field-cage, comprised of a stack of 60 field-shaping electrodes of decreasing voltage from bottom to top. The design is completed by the external cryostat and signal feed-through elements called chimneys, which put in contact the internal electronic with the outside of the tank. A 3D module of the entire structure is shown in Figure 2.17.

### 2.2.3 LBNF beamline

The LBNF BeamLine at Fermilab is a horn-focused, sign-selected neutrino beam, designed to meet the DUNE's long-baseline physics requirements [49]. It is aimed towards the South Dakota facilities hosting the Far Detectors, 1480m underground and 1300 km away from the FNAL facilities.

The main components of the beamline are shown in Figure 2.19. A primary beam of accelerated protons (60-120 GeV) is produced in the Fermilab Main Injector (MI) (the primary beam main specifications and characteristics for 12 GeV protons are listed in Table 2.1). It is then extracted and transported through a man-made hill, at the apex of which it is bent downwards, toward a target at ground level, in the LBNF Target Hall. The total bend amounts

Parameter	Value
Energy	120 GeV
Protons per cycle	$7.5 \times 10^{13}$
Spill duration	$1.0 \times 10^{-5}$ s
POT per year	$1.1 \times 10^{21}$
Cycle Time	1.2 s
Beam Power	1.2 MW
Beam size at target	1.5-1.7 mm
$\Delta p/p$	$11 \times 10^{-4}$ 99% ( $28 \times 10^{-4}$ 100%)
Transverse emittance	$30\pi \mu m$ 99% ( $360\pi \mu m$ 100%)
Beam divergence (x,y)	15-17 $\mu rad$

Table 2.1: Summary of the main primary proton beam parameters [49]

to  $7.2^\circ$  westward and  $5.4^\circ$  downwards and directs the flux toward the Far Detectors.

When the accelerated protons hit the target, mesons are generated; these are then focused by magnetic horns into a decay pipe where they decay into muons and neutrinos. The decay pipe is 194 m long in total, with an additional 27 m acting as the target chase. The focusing structure, consisting of the two NuMI horns (placed 6.6m apart and set at 230 kA ), provides neutrinos in the energy range 0.5-5 GeV range, which is enough to cover the first

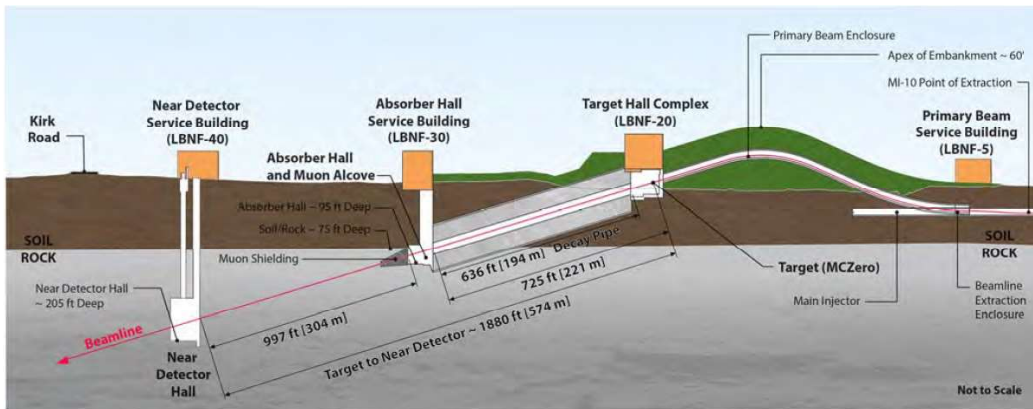


Figure 2.19: Schematic representation of the LBNF neutrino beamline facilities at Fermilab [49]

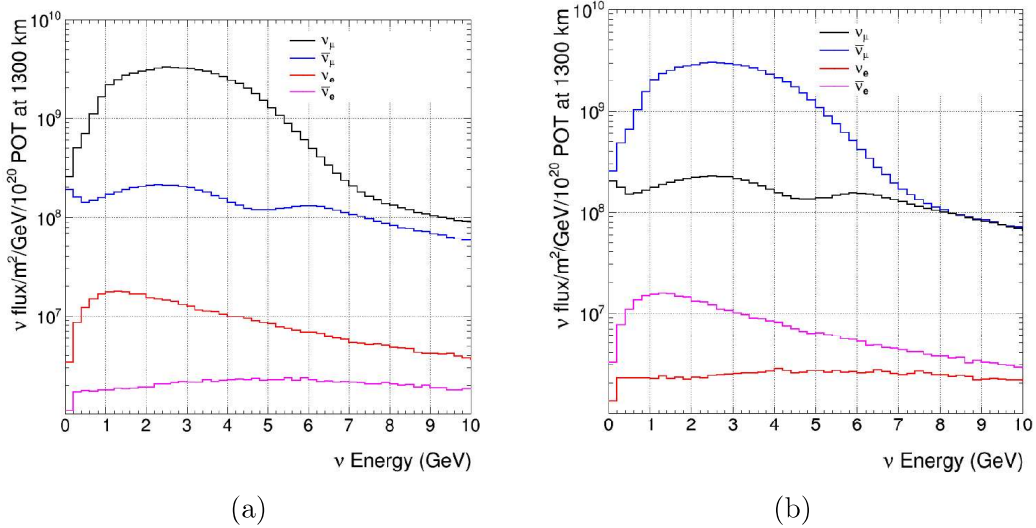


Figure 2.20: Expected neutrino and antineutrino beam produced focusing positive (a) and negative (b) mesons. [49]

two oscillation nodes (for a 1300 km baseline 2.4 and 0.8 GeV respectively). The facility is set to run initially with a power of 1.2 MW (later upgrading to 2.4MW), corresponding to  $1.1 \times 10^{21}$  protons-on-target (POT) per year, for 120 GeV protons. This assuming that  $7.5 \times 10^{13}$  protons are produced for each 1.2 s MI cycle and a total efficiency of 0.56 for the entire focusing and transportation in LBNF.

The neutrino and antineutrino expected fluxes obtained focusing positive and negative particles are shown in Figure 2.20.

### 2.2.4 The near detector

The near detector will be located in the Fermilab facilities a few hundred meters away from the NuMI beam source. It will consist of two movable systems, capable of being positioned both on and off-axis, and a fixed one that will always be on axis. The two movable detectors will both be based on Argon as a target, an essential characteristic for evaluating the systematics on the Far detector's physics response. One of them will contain liquid Argon, while the other will be based on a high pressure Argon TPC design. The liquid argon TPC will be called ArgonCube and will feature a modular design and a fully pixelated charge readout[51]. The advantages of segmenting a large LArTPC are a reduction in drift voltage requirements and a lessened focus on Argon purity. This in turn reduces risks related to electric breakdown and purity losses. The pixelated charge readout provides an

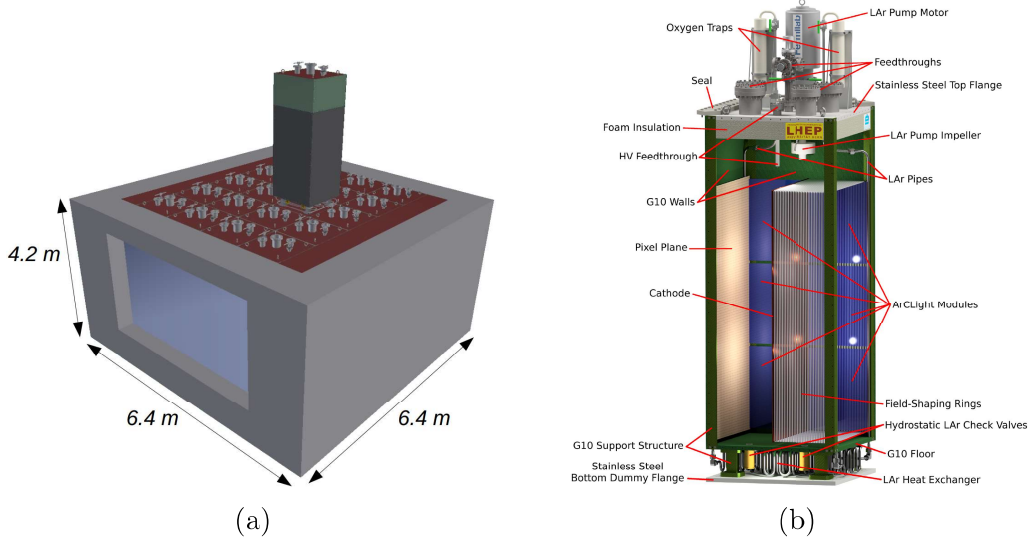


Figure 2.21: Schematic design of ArgonCube (a) and one of its modules (b) [52]

unambiguous event topology reconstruction, which is vital in cases of events with high multiplicity and possibility of pile-up. In Figure 2.21 a geometric representation of ArgonCube with a cross section of one of its modules is presented.

The second movable detector, known HPgTPC (High Pressure gas TPC) is a magnetized spectrometer based on high pressure Argon TPC technology, surrounded by an electro-magnetic calorimeter [53]. Its main purpose will be to tag muons and the sign of charged particles exiting ArgonCube, thanks to its optimal tracking efficiency, particle identification, momentum and angular resolution. HPgTPC will also be extremely useful in detecting charged particles of very low energy from  $\nu$  interactions in gas.

The fixed detector will reuse parts of a previous detector named KLOE, today situated at the Laboratori Nazionali di Frascati (LNF) and will take the name SAND [54]. The specific purpose of this detector in its Straw Tube Tracker (STT) configuration, one of the two currently being considered, will be discussed in the next Chapter [55].



# Chapter 3

## SAND

### 3.1 Requirements

The general formula for the number of events for a process X, both in the Near and Far detectors is:

$$N_X(E_{rec}) = \int_{E_\nu} dE_\nu \Phi(E_\nu) P_{osc}(E_\nu) \sigma_X(E_\nu) R_{phys}(E_\nu, E_{vis}) R_{det}(E_{vis}, E_{rec}) \quad (3.1)$$

$\Phi$  is the incoming neutrino flux,  $\sigma_X$  is the cross section of the process on a given nucleus,  $R_{phys}$  is the physics response introduced by nuclear smearing and  $R_{det}$  is the detector acceptance for the final state particles.  $E_\nu$ ,  $E_{vis}$  and  $E_{rec}$  are the neutrino true energy, the total energies of the visible final state particles and the final reconstructed energy. The main terms in the expression need to be unfolded. This is not possible by using only one detector and one nuclear target.

The main goal of the ND will be to provide constraints on all the systematic uncertainties relevant for the oscillation analysis. The basic requirement is that the combined systematics must be smaller than the correspondent statistical uncertainties. To this end a detailed knowledge of the neutrino interactions in Argon is needed, since the far detectors will be a LArTPC. Since DUNE will operate over a wide energy range ( $0.5 < E_\nu < 10$  GeV), this includes contributions from all the main neutrino processes:  $\sim 25\%$  quasi-elastic (QE), 42% resonances (RES) and 33% deep inelastic scattering (QES), the most critical regions being the one related to resonances and the transition region to DIS. The ND complex as it's currently planned can provide sufficiently precise measurements for neutrino and anti-neutrino interactions in Ar. This will be possible thanks to the combination of the high mass LArTPC ArgonCube ( $\sim 25$  tons), which will offer a large statistics of

events detected using a technology similar to the FD, and a High Pressure Ar gas TPC (HPgTPC), which will be able to detect low threshold particles. Utilizing Ar as the sole nuclear target in the ND complex though would cause severe limitations. The Argon nucleus is not a good target for flux measurements  $\Phi(E_\nu)$ , since the nuclear effects on the final state are significant. The nuclear smearing factor  $R_{phys}$  is also rather large, introducing significant modifications in the spectrum reconstruction. A characterisation of these effects using only Ar as a target is impossible, since the factors in eq. 3.1 cannot be decoupled. This fact introduces irreducible systematics and forces a large reliance on Montecarlo and model corrections. This is particularly problematic when searching for new physics, since new unexpected signals could be eliminated by ad-hoc tunings of the models.

SAND has been designed to offer a solution to these problems. It will not only offer a variety of nuclear targets, but thanks to its Straw Tube Tracker (STT) it will be able to reach the levels of precisions needed to constrain the systematic uncertainties for the oscillation measurements, while also having an independent physics program.

## 3.2 Detector components

SAND aims to be a compact detector capable of calorimetry and precision tracking on events produced on different materials such as Argon and Hydrogen. The original KLOE electromagnetic calorimeter (ECAL) and magnet will be reused, while the inner tracking region will be replaced. The tracker design considered in the scope of this thesis is based on straw tube technology with the addition of a small liquid Argon region used for inter-calibration: the LAr meniscus.

### 3.2.1 KLOE's magnet

SAND will reuse the existing superconducting magnet employed by KLOE [56]. Together with its iron yoke it produces a magnetic field of 0.6 T over a cylinder of 4.8 m of diameter and 4.3 m of length. This is achieved by applying 2902 A of current to a coil, located inside a cryostat (a hollow cylinder with 90 cm thick walls, 5.76m in total diameter and 4.40m long), positioned inside an iron yoke. Specifically the coil is a single conducting layer, consisting of Rutherford (Rb-Ti) cables co-extruded with high purity aluminium, held in an aluminium supporting cylinder with cooling channels welded on the outside.

The cooling of the coil is performed employing thermo-syphoning cycles,

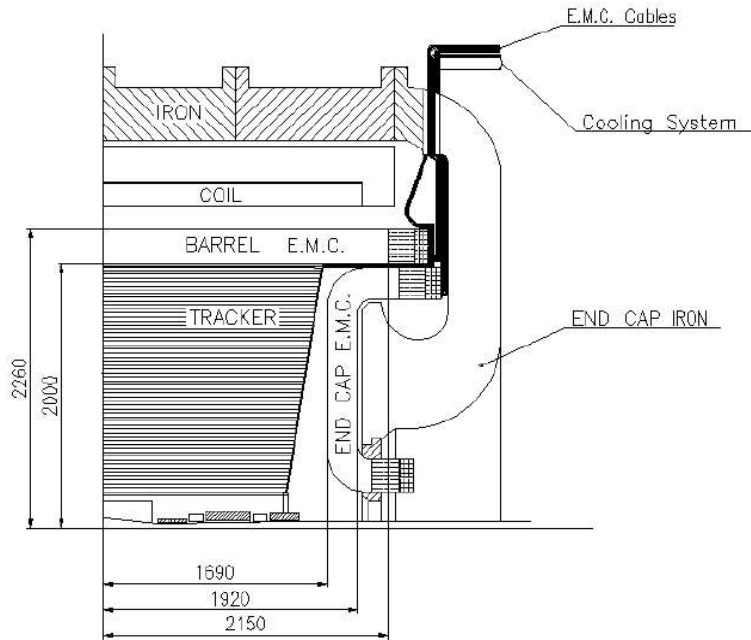


Figure 3.1: Cross section of the KLOE detector. The lengths are shown in mm. [55]

while the current leads are cooled with liquid helium and the radiation shields using gas-He at 70K for a total cold mass of  $\sim 8.5$  tons. New cryogeny solutions are being evaluated at the moment.

A section of KLOE's structure is shown in Figure 3.1.

### 3.2.2 KLOE's electro-magnetic calorimeter

The KLOE electro-magnetic calorimeter (ECAL) is a sampling calorimeter made of lead and scintillating fiber which offer timing resolution under the ns range, good light transmission and great hermeticity [56]. It will also be reused as SAND's calorimeter. The barrel calorimeter is a cylinder segmented into twenty four trapezoidal modules 4.3 m long, 23 cm thick and bases of 52 and 59 cm. The ECAL is completed by two end-caps, divided into vertical modules of variable width and height between 0.7 m and 3.9 m and 23 cm thick. The end-cap modules are bent horizontally to place the photo-tubes in parallel with the magnetic field and ensure the absence of inactive gaps.

The modules are read by photo-tubes connecting to photo-guides at both ends of the modules. The read-outs are divided into five planes, the first four being 4.4 cm deep and the last being 5.4 cm deep, each being subdivided

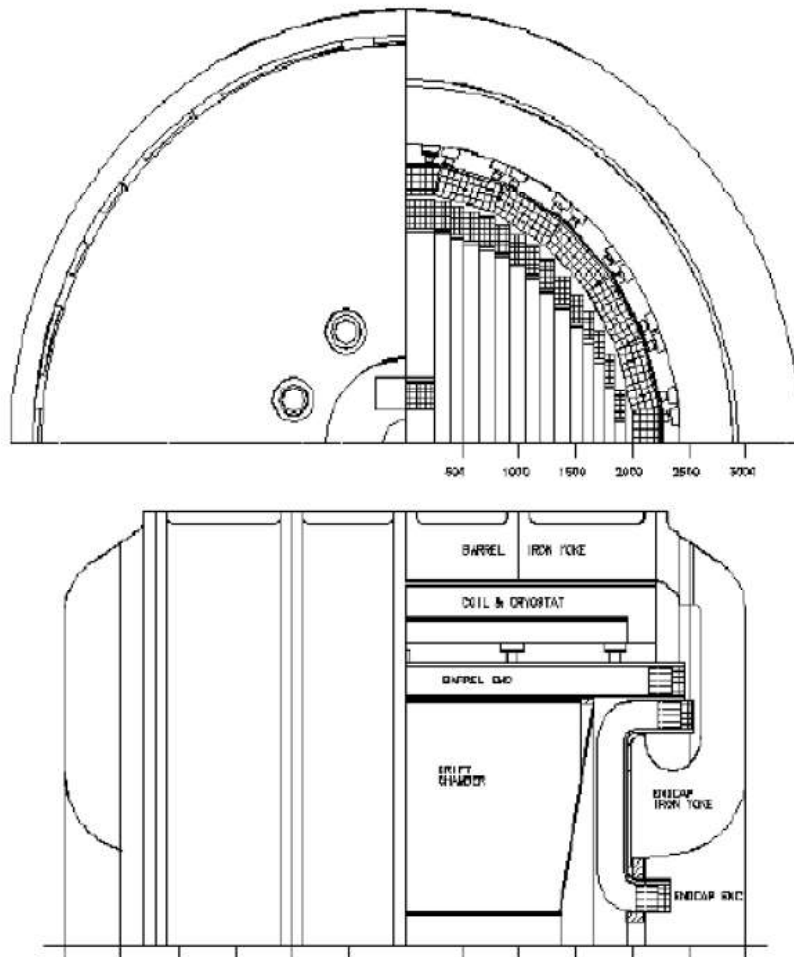


Figure 3.2: Schematic cross section of KLOE showing the calorimeters from the front (top figure) and side (bottom figure). The segmentation at the ends of the calorimeters is made to portray the light-guides. The lengths are shown in mm. [55]

into 4.4 cm elements, one for each light-guide.

The spacial, energetic and timing resolution evaluations performed during KLOE's commissioning and running phase amount to:

- $r - \phi$  or  $x - z$  spacial resolution determined by the read-out segmentation: 1.3 cm ( $44/\sqrt{12}$  cm)
- Energy resolution:  $\sigma/E = 5\%/\sqrt{E(\text{GeV})}$
- Timing resolution:  $54/\sqrt{E(\text{GeV})}$  ps

Figure 3.2 shows the layout of the ECAL with the light read-out segmentation.

### 3.2.3 The inner tracker

The inner tracker's design specifications are directly dictated by the necessities of the physics goals of the Near Detector:

1. High granularity to guaranty high resolution in momentum, angle and space, maintaining a low density and an overall thickness of about one radiation length  $X_0$  to minimize secondary interactions;
2. Providing a large target for neutrino interactions, with a fiducial mass of the order of  $\sim 5$  tons;
3. Capability to offer a range of different materials as target;
4. Particle identification for  $e, \pi, K, p, \mu$ ;

The first two goals in particular seem to be in contrast with one another requiring at the same time a large target mass and a high precision and low density tracking system.

The solution opted by the SAND STT design is to separate the neutrino targets from the tracking system, which are then negligibly light weight with respect to the former. To preserve a low density and achieve the goal of maintaining the detector transparent to secondary particles, the target is spread over the detector in smaller modules. This also makes the goal of having different target materials more easily achievable.

### The straw tube tracker

One of the two main proposed design now in discussion to achieve the previously detailed goals is a tracker based on low-mass straw tube technology, to be positioned inside KLOE's magnet. The Straw Tube Tracker (STT) would be built in a compact modular fashion, each module being 43.8 mm thick and containing:

- Four straw layers disposed in a XXYY configuration. Each straw would be 5 mm in diameter and made of 1000 Angstrom Al coated mylar, containing a tungsten wire 20  $\mu\text{m}$  in diameter. These would constitute the tracking component of the detector and would contribute to only 5% of the total mass, having an average density of  $\rho \sim 0.17 \text{ g/cm}^3$  and a radiation length of  $X_0 \sim 2.5 \text{ m}$ ;
- A polypropylene  $\text{CH}_2$  solid target slab of 5 mm, whose thickness can be adjusted according to the desired detector mass;
- A transition radiation (TR) radiator composed of 150 polypropylene 15  $\mu\text{m}$  thick foils, separated by 120  $\mu\text{m}$  gaps, occupied by a standard  $\text{Xe}/\text{CO}_2$  70/30 gas mixture. This specifically optimizes the  $e/\pi$  separation;

A graphical representation of a section of a STT module is shown in Figure 3.3. Both the polypropylene target and the TR radiator are removable components and can be substituted with a variety of targets. The most important alternative target would be graphite, which is crucial for the measurement of the C background in hydrogen interactions. A 4 mm graphite slab, placed in the same position as the  $\text{CH}_2$  target slab, would be enough to maintain the same combined  $X_0$  of both the polypropylene slab and the radiator. Of the 82 total modules of the STT, the standard  $\text{CH}_2$  modules would be interleaved with 9 graphite ones, in its standard configuration. This would amount to a total of 677 kg of hydrogen targets and 528 kg of carbon targets.

Another important target material is Ca. This could be implemented in the upstream modules much in the same vein as for the graphite. Calcium is important because is isoscalar to Ar allowing a complete characterization of  $A=40$  nuclei, while also enabling various isospin measurements. Many other materials such as Pb and Fe could be implemented, according to the needs of the collaboration.

The STT modules support frames need to provide an adequate mechanical support, while also adding a minimal amount of mass. A good compromise can be achieved with a design based on U-shaped beams made of C-composites, so that the  $X_0$  traversed by the secondary particles is minimal.

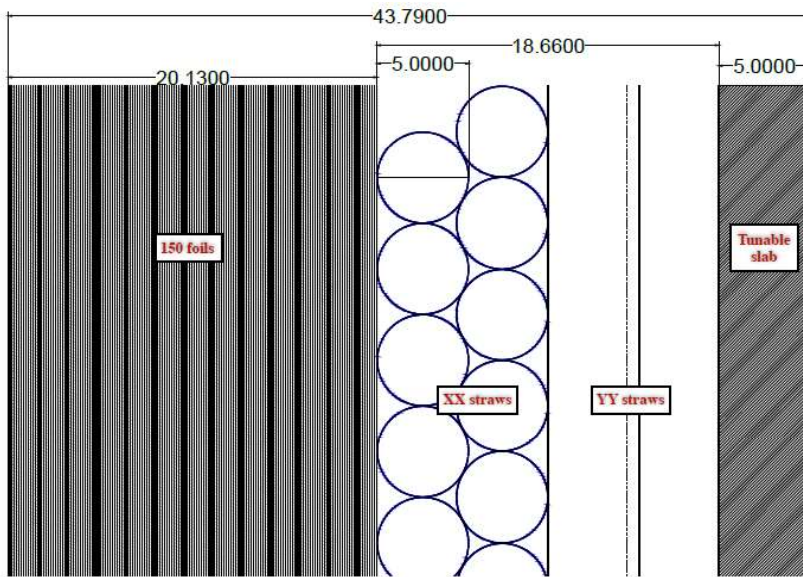


Figure 3.3: Section of an STT module with its three main components. From left to right: a TR radiator made of 150 foils of polypropylene; four straw tube layers in a XXYY disposition; a  $\text{CH}_2$  tunable target.

The STT design is overall very well equipped to provide for the physics goals set for SAND. It provides a very good spatial ( $< 200\mu\text{m}$ ), angular ( $\sim 2$  mrad), momentum ( $\sim 3\%$ ) and timing (important for resolving the beam structure) resolutions, while also offering good particle identification by exploiting both the ionization  $dE/dx$  and TR for the  $e/\pi$  separation. The polypropylene targets, in addition, offer a clean hydrogen target for the neutrino interactions, while also being easily interchanged with other materials at need. An additional small liquid Argon target is also added to the design.

### The liquid Argon meniscus

The presence of a small component of liquid Argon in SAND, is essential to understand the nuclear effects of the material that will constitute most of the Far Detector. This meniscus of LAr should be small enough to keep energy loss, showering and multiple Coulomb scattering to a minimum. While the exact position and dimension of this component are still in a phase of optimization, recent designs suggest a volume positioned upstream, almost in direct contact with the ECAL. It will require an additional cryostat system and will be equipped with scintillation light readout systems.

## 3.3 Physics Program

### 3.3.1 Reducing the systematics

In order to constrain the systematic uncertainties for the oscillation measurements that DUNE will have to perform, all the variables that enter in eq. 3.1 need to be decoupled and measured independently:

- $\Phi(E_\nu)$ : the flux measurements benefit from low A targets and low density to achieve a high resolution. Both goals are achieved by the STT thanks to the polypropylene targets and the low mass of the straw tubes planes.
- $R_{phys}(E_\nu, E_{vis})$ : to disentangle the physics response from  $R_{det}$  one needs to have in the same detector Ar, H and other light elements targets. The design of the STT modules and the introduction of the LAr meniscus provide all the necessary nuclei.
- $\sigma_X(E_\nu)$ : once the flux is precisely measured, the cross section on Argon can be evaluated by SAND by using the large sample offered by interactions in the LAr and HPgTPC. Precise cross section measurements require a good characterisation of  $R_{phys}R_{det}$
- $R_{det}(E_\nu, E_{vis})$ : the FD detector response can be evaluated only by measurements performed in the LAr ND. The STT offers a determination of  $\sigma_X R_{phys}$  by the possibility of comparing interactions on H and Ar, which makes the extraction of  $R_{det}$  straightforward.

A detailed characterization of the neutrino fluxes is a necessary condition for all measurements involving the near and far detector, and for the unfolding of the terms in eq. 3.1. SAND will determine both absolute  $\nu_\mu$ ,  $\bar{\nu}_\mu$  and relative  $\nu_\mu$ ,  $\bar{\nu}_\mu$ ,  $\nu_e$ ,  $\bar{\nu}_e$  fluxes through a series of measurements of different processes, the most important of which are the ones with hydrogen atoms and electrons. The STT provides a large quantity of hydrogen targets.

Once the fluxes  $\Phi(E_\nu)$  are measured, the other three parameters  $\sigma_X R_{phys}R_{det}$  need to be unfolded. The unfolding of  $\sigma_X R_{phys}$  requires that both Ar and lighter targets are present in the same detector, so that  $R_{det}$  is the same between measurements. In particular for hydrogen targets we have  $R_{phys} = 1$ , which means that the cross-section on H can be accurately measured and the unfolding of the neutrino energy depends only on  $R_{det}$  which is defined by  $\delta p/p$ . Comparing that with interactions on Argon in STT allows for the determination of  $\sigma_X R_{phys}$ .

To constrain  $R_{phys}$  separately one can define a set of kinematic variables

sensitive to nuclear smearing, and compare the distributions of these observables in CC interaction samples on Ar and H. This strategy allows for a full determination of nuclear smearing effects with the neutrino spectrum seen by the ND, which is different from the one in the FD. For this reason it is essential to measure a complete set of kinematic variables, in order to resolve potential degeneracies.

The measurement of  $\sigma_X R_{phys}$  and the constraints on  $R_{phys}$  offered by SAND can then be compared with the measurements made in the LAr ND ArgonCube to unfold  $R_{det}$  in liquid Argon and to validate the predictions for the FD.

### 3.3.2 Precision measurements and new physics

The high precision of the SAND detector and the uniqueness of neutrinos as probes of fundamental interactions allow for an independent physics program of precision measurements and searches for new physics. In this section some of the opportunities presented by this broad physics program are outlined.

#### Precision measurements in the electro-weak sector

The characteristics of SAND allow for an improvement on the previous best measurements of the weak mixing angle ( $\sin^2 \theta_W$ ), performed by the NuTeV experiment in neutrino DIS interactions [58]. The measurement of this parameter in SAND would provide a direct determination of the coupling of the neutrinos with  $Z^0$  while at the same time probing a different momentum transfer scale than LEP.

The DUNE ND complex could measure  $\sin^2 \theta_W$  from the ratio of NC and CC neutrino DIS interactions  $\mathcal{R} = \sigma_\nu^{NC}/\sigma_\nu^{CC}$ . The high resolution of the STT and the efficiency of the determination of electron neutrino CC interactions and of the separation of NC and CC events via kinematic analysis, would allow for a substantial improvement on previous experiments' systematics and overall precision. The uncertainties in the determination of  $\mathcal{R}$  would be dominated by the ones introduced by the theoretical models used for the the structure of the nuclear targets.

A separate channel for the determination of the weak mixing angle is the  $\nu_\mu e$  NC elastic scattering, which would be uneffected by nuclear model uncertainties, but would be limited in statistics by the small cross section of the process. In particular the observable used would be the ratio between neutrino and antineutrino NC interactions  $\mathcal{R}_{\nu e} = \sigma(\bar{\nu}_\mu e \rightarrow \bar{\nu}_\mu e)/\sigma(\nu_\mu e \rightarrow \nu_\mu e)$ . This measurement is characterized by a totally different momentum transfer

scale from the one performed measuring the neutrino DIS interactions. This would allow for a test on the running of  $\sin^2 \theta_W$ .

### Isospin physics tests

The availability of large statistics of neutrino-hydrogen interactions in SAND allows for the testing of isospin sum rules, which at the moment suffer from low statistics. These include the Adler sum rule  $S_A = 0.5 \int_0^1 dx/x(F_2^{\bar{\nu}p} - F_2^{\nu p}) = I_P$  [59], which gives the isospin of the target and the Gross-Llewellyn-Smith(GLS) sum rule  $S_{GLS} = 0.5 \int_0^1 dx/x(xF_3^{\bar{\nu}p} - xF_3^{\nu p})$  [60]. Both could be measured as a function of the momentum transfer  $Q^2$  in neutrino and anti-neutrino interactions on hydrogen from the respective structure functions, which in turn could be determined from the corresponding differential cross-sections. The measurement of  $S_A$  in particular would be sensitive to violation of isospin symmetry, charm production and strange sea ( $s - \bar{s}$ ) asymmetries. Thanks to the combination of nuclear and proton (H) targets SAND is also capable of testing isospin charge symmetry (which implies that  $F_{2,3}^{\bar{\nu}p} = F_{2,3}^{\nu n}$  and for isoscalar targets  $F_{2,3}^{\bar{\nu}} = F_{2,3}^{\nu}$  ).

### Strangeness measurements of the nucleus

While the strange quark vector elastic form factors have been precisely measured in parity-violating electron scattering experiments, the strange component of the axial-vector form factors  $G_A^s$  are not yet well determined. SAND will have access to this parameter from measurements of NC elastic scattering off protons  $\nu_\mu(\bar{\nu}_\mu) + p \rightarrow \nu_\mu(\bar{\nu}_\mu) + p$ . The differential cross section for this process is proportional to the axial vector form factor in the limit that  $Q^2 \rightarrow 0$ :

$$\frac{d\sigma}{dQ^2} \propto G_1^2 = \left( -\frac{G_A}{2} + \frac{G_A^s}{2} \right)^2 \quad (3.2)$$

$G_A$ , which is the known axial form factor, can be determined by SAND by measuring the ratio of the NC elastic and quasi-elastic processes over a large  $Q^2$  range:  $\mathcal{R}_{\nu(\bar{\nu})p} = \sigma(\nu_\mu(\bar{\nu}_\mu)p \rightarrow \nu_\mu(\bar{\nu}_\mu)p)/\sigma(\nu_\mu(\bar{\nu}_\mu)n(p) \rightarrow \mu^-(\mu^+)p(n))$ . Note that the determination of  $G_A^s$  also represents the most direct method of measuring the value of the nucleon spin  $\Delta s$ , since for  $Q^2 = 0$  we have that  $G_A^s \rightarrow \Delta s$ .

The resolution of the STT also renders SAND capable to do precise measurements of charmed mesons decay modes, such as the  $\mu\mu$  and  $\mu e$  semi-leptonic charmed decay channels. The study of charm production resulting from  $\nu$  and  $\bar{\nu}$  interactions with the nuclei, offers a direct probe into the strangeness content of the nucleons [61].

## Nucleon structure and QCD studies

SAND will offer a precise calibration of energy scale uncertainties and high precision measurements of neutrino and antineutrino fluxes. This allows for a determination of nucleon structure functions  $F_2, xF_3, F_L, F_T$  using neutrino neutrino and antineutrino DIS interactions. Parton Distribution Functions (PDFs) as well as perturbative and non-perturbative corrections could also be studied performing global QCD analyses over a broad range of  $Q^2$  and Bjorken  $x$ . The presence of both Hydrogen and nuclear targets in SAND are essential to separate valence and sea quarks distributions,  $d$  and  $u$  distributions as well as  $s$  and  $\bar{s}$  distributions.

## Neutrino-nucleus interaction studies

The modular structure of STT allows for the integration of many different nuclear target. This creates the possibility of studying how the nucleon structure is modified inside a heavy nucleus, by measuring structure functions, form factors and cross-sections. The study of final state interactions is also important, since they can introduce a significant smearing in the reconstruction of the kinematics variables of the final state particles.

## New physics searches

All the precision measurements described in the present are potentially sensitive to many BSM (Beyond the Standard Model) effects which would manifest as deviations from the SM predictions. Sand is also capable of more direct searches for new physics. One possible field of study would be the test of the MiniBooNE low energy anomaly at different but similar  $L/E$ . SAND would be particularly well set for the task thanks to the electron identification capability and high resolution of STT.

The oscillation into sterile neutrino explanation for the MiniBooNE anomaly could be tested by measuring the CC ratios for both neutrinos and antineutrinos  $\mathcal{R}_{e\mu} = (\nu_e N \rightarrow e^- X) / (\nu_\mu N \rightarrow \mu^- X)$  and  $\bar{\mathcal{R}}_{e\mu} = (\bar{\nu}_e N \rightarrow e^+ X) / (\bar{\nu}_\mu N \rightarrow \mu^+ X)$  as well as the NC/CC ratio  $\mathcal{R}_{\nu(\bar{\nu})p}$  as a function of  $L/E$ . These measurements would be sensitive to both appearance and disappearance anomalies in all four neutrino spectra. STT would also be sensitive to  $\nu_\tau$  appearance, which could result from both sterile neutrino oscillations or BSM interactions. SAND would also enhance the sensitivity of the ND to dark sector physics. This includes heavy sterile neutrino searches ( of the type proposed in the see-saw mechanism ), axions, dark photons, WIMPs and many others.

